Pre-patterned epithelial invagination prevents mechanical instability during fly gastrulation

Bruno C. Vellutini[1,*] Marina B. Cuenca[1] Abhijeet Krishna[1,2,3]
Alicja Szałapak[1,2,3] Carl D. Modes[1,2,3] Pavel Tomančák[1,3,*]

[1] Max Planck Institute of Molecular Cell Biology and Genetics, Dresden, Germany
[2] Center for Systems Biology Dresden, Dresden, Germany
[3] Cluster of Excellence Physics of Life, Technische Universität Dresden, Dresden, Germany

[*] Correspondence: Bruno C. Vellutini <vellutini@mpi-cbg.de>, Pavel Tomančák <tomancak@mpi-cbg.de>

Abstract

The cephalic furrow is a deep epithelial fold that demarcates the head–trunk boundary of fly embryos during gastrulation. It forms under strict genetic control using active cellular mechanisms and follows an invariant morphogenetic sequence. But unlike other embryonic invaginations, the cells that invaginate in the cephalic furrow do not give rise to any precursor tissues or larval traits. The cephalic furrow is transient and unfolds leaving no trace. For these reasons, its function during development has remained elusive. Here we show that the cephalic furrow plays a mechanical role during *Drosophila* gastrulation. By live-imaging mutant embryos, we find that without the cephalic furrow, ectopic folds appear around the head–trunk interface indicating that the epithelial stability has been compromised. Using *in vivo* perturbations and *in silico* simulations, we demonstrate that ectopic folding in cephalic furrow mutants occurs due to the concomitant formation of mitotic domains and extension of the germ band. These events increase the tissue strain in the head–trunk interface giving rise to mechanical instabilities. Further, we show by simulations that an early pre-patterned invagination can effectively prevent the build-up of compressive stresses by retaining epithelial tissue out-of-plane before other morphogenetic movements take place. Our findings suggest the cephalic furrow absorbs compressive stresses at the head–trunk boundary during fly gastrulation, and raise the hypothesis that mechanical forces may have played a role in the evolution of the cephalic furrow.

Main

Epithelial folding is a fundamental process of animal embryogenesis[1]. Tissues fold through intrinsic cellular mechanisms or extrinsic tissue-scale forces[2]. In pre-patterned invaginations, the position and timing of folding is tightly regulated by genes which instruct active cell shape changes driving morphogenesis[3]. In fly embryos, the epithelial invaginations that form during gastrulation are pre-patterned and usually fulfill a clear role in development: giving rise to precursor tissues. The ventral furrow and the midgut invaginations, for instance, give rise to the mesoderm and to the endoderm of the flies, respectively. One exception to this pattern is a prominent head invagination present in flies, known as the cephalic furrow.

The formation of the cephalic furrow is one of the earliest events in *Drosophila* gastrulation. It first appears as a lateral indentation which quickly invaginates and forms a deep epithelial fold at the

boundary between head (procephalon) and trunk (germ band)[4–6]. Similar to other embryonic invaginations, the formation of the cephalic furrow is under strict genetic control and follows a stereotypic morphogenetic sequence of events. The site of invagination is determined by the zygotic expression of two transcription factors, *buttonhead* (*btd*) and *even skipped* (*eve*), whose domains overlap at the head–trunk boundary by a narrow row of blastoderm cells[7]. These so-called initiator cells shorten along the apical–basal axis by activating lateral myosin contractility and drive the infolding of the tissue[8]. The position of the cephalic furrow is specified with remarkable accuracy[9]. Once initiated, the mechanical coupling between invaginating cells ensures the precision of the tissue fold during morphogenesis[8]. The resulting fold spans the entire lateral surface, from dorsal to ventral, making the cephalic furrow a distinguishable landmark of the embryo during gastrulation[4,5]. This prominent fold, however, is only transient. A couple of hours after gastrulation, the cephalic furrow unfolds and disappears leaving no trace, and the invaginated tissue does not give rise to any specific precursors or larval structures[4]. The cephalic furrow is, therefore, a puzzling structure; it is a prominent fold forming at a crucial stage of development, has a finely regulated morphogenesis driven by active cellular mechanisms, but vanishes without any obvious function for the embryo.

This ephemeral nature and absence of associated fates suggests the cephalic furrow may play a more immediate, physical role during gastrulation. Some hypotheses are that the invagination functions as a temporary storage of anterior cells until later in development[10], or that the invaginated cells anchor anterior tissues and help directing tissue flow during gastrulation[11,12]. The cephalic furrow retains a significant number of blastoderm cells beneath the surface of the embryo during gastrulation (about 10% according to recent estimates[13]), but what function such storage accomplishes remains unclear, and none of these hypotheses have been investigated *in vivo*.

Our work investigates the physical consequences of perturbing the formation of the cephalic furrow in *Drosophila*. To comprehend the impact of cephalic furrow defects, we generated fluorescent lines carrying a membrane marker and a loss of function allele for genes known to affect cephalic furrow formation—*btd*, *eve*, and *paired* (*prd*)[7,14]. In *prd* mutants, the formation of the cephalic furrow is delayed relative to wildtype embryos[14], while in *btd* and *eve* mutants, the cephalic furrow is absent[7]. To capture the tissue dynamics during gastrulation and the relative timing of developmental events, we imaged these mutant embryos using lightsheet microscopy *in toto* and with high temporal resolution.

Our recordings show differences between the three mutants at the cellular and tissue levels (Figure 1a). In wildtype embryos, the initiator cells undergo cell shortening and anisotropic apical constriction at the end of cellularization[6] (Figure S1a,b). These behaviors are delayed but still present in *prd* mutants. The initiator cells in *prd* mutants lack the typical arched profile of the wildtype initiators, but they shorten and apically constrict forming a clear infolding point in the epithelium about six minutes after gastrulation (Figure S1a,b). The putative initiator cells of *btd* mutants do not shorten, but show a reminiscent degree of apical constriction which creates a small indentation in epithelium of some embryos (Figure S1a,b, Video S1). In contrast, *eve* mutants show neither apical constriction nor cell shortening and the epithelium remains flat until about ten minutes after gastrulation (Figure S1a,b). While the behavior of initiator cells is perturbed in the three mutants, it is only in *btd* and *eve* that the cellular basis for cephalic furrow formation—the cell shortening—is severely disrupted. Strikingly, about 10–15 min after the onset of gastrulation, these mutants form a notable epithelial fold near the canonical position of cephalic furrow formation (Figure 1b,c, Figure S1a). Intrigued by this puzzling phenotype, we asked whether the formation of this late fold is a direct consequence of the absence of the cephalic furrow.

The appearance of a late fold was first noted in *eve* mutants[7], and only more recently observed in *btd* mutants[8]. However, their significance and the mechanisms driving their formation have remained unclear. Our recordings show that in all embryos where the cephalic furrow fails to initiate, ectopic folds appear near the canonical site of cephalic furrow invagination (Figure 1a,b,c, Video 1, Video 2). They appear 15 min after the cephalic furrow would have formed, when the germ band is extended to

around 35% of the egg length (Figure 1a,c,d, Table 1), and then disappear in about 20 min—faster than the wildtype cephalic furrow. Ectopic folds have a wider and often asymmetric cleft compared to the cephalic furrow, and lack the typical cell morphologies of the invagination, such as the wedge-shaped initiator cells and elongated edge cells[6] (Figure 1b, Video 3, Video 4). Unlike the cephalic furrow, the position of ectopic folds varies between individual mutant embryos as they can form anterior, posterior, or near the wildtype site of invagination (Figure 1f, Figure S2b, Video S2, Video S3). Finally, ectopic folds show more variable kinetics (Figure S2d,e), are 25% shallower (Figure S2f), and occupy an area 50% smaller compared to the cephalic furrow (Figure 1g,h, Figure S2c). Such differences in morphology and dynamics suggest that the cephalic furrow and the ectopic folds form via distinct mechanisms.

To better understand the mechanisms of ectopic folding, we analyzed the phenomenon more broadly in our datasets and found that ectopic folds may also occur in embryos with a cephalic furrow (i.e. *btd* or *eve* heterozygotes, *prd* hetero- or homozygotes, and wildtype). These ectopic folds, however, differ from the ectopic folds of cephalic mutants in two key aspects. While the frequency of ectopic folding is high in cephalic furrow mutants (>93%)—nearly every *btd* and *eve* homozygote shows one or more ectopic folds per embryo side (2.0±1.0 and 1.8±0.6, respectively) (Figure 1b, Figure S2a)—the frequency of ectopic folding in the other embryos is lower, ranging between 12% (*eve* heterozygotes) and 80% (wildtype embryos) (Table 2). In addition, the area of ectopic folds in wildtype embryos is 3–4x smaller than the area of ectopic folds in cephalic furrow mutants (Figure S2g–k, Table 3). Thus, cephalic furrow mutants have more frequent and more prominent ectopic folds compared to wildtype embryos. These data provide evidence that the absence of the cephalic furrow is causally linked to an increase in the frequency and in the magnitude of ectopic folding during *Drosophila* gastrulation.

The variable positions and frequency of ectopic folding suggests that they are not under genetic control comparable to that of the cephalic furrow, but that they may form as a result of physical interactions in the tissue. We investigated two concurrent gastrulation processes that could drive their formation: cell divisions in mitotic domains and the extension of the germ band. Mitotic domains are groups of blastoderm cells that divide in synchrony during the cleavage cycle 14[5]. The first mitotic domains in *Drosophila* appear in the head around 20 min after gastrulation[5] which coincides with the formation of ectopic folds (Figure 1a,c,d). Ectopic folds always appear in between or adjacent to mitotic domains (Figure 2a). The dividing cells synchronously lose their basal attachment, round up at the apical side, and more than double (2.3x) their apical area during anaphase elongation (Figure S3). This expansion compresses the adjacent non-dividing cells which are the first to infold, followed by a portion of the dividing cells within mitotic domains (Figure 2b). Mitotic expansions always precede ectopic folding (Figure 2c, Figure S1a). Compared to the progressive invagination of the cephalic furrow (about 14 min), the process of ectopic fold formation is abrupt (about 4 min) (Figure S1a, Video 5). To understand the dynamics of tissue strain, we measured the rate of tissue deformation (strain rate) at the head–trunk using particle image velocimetry. We find that *btd* mutants show a strain rate 1.3x higher than sibling controls with a peak that coincides with the maximum expansion of mitotic domains and with the appearance of the ectopic folds (Figure 2d,e, Figure S4, Video 6). However, for the ectopic folds that often form posterior to the Mitotic Domain 6 (MD6) (Figure 2a,c), the source of compression must be different; we hypothesized the germ band is contributing. Therefore, we have also quantified the strain rate at this posterior region where the trunk tissue interacts with the tip of the germ band (trunk–germ). At this trunk–germ interface, the strain rate is lower than at the head–trunk, but it steadily increases over time probably driven by the extending germ band (Figure 2d). The epithelial cells between MD6 and the germ band tip are indeed more compressed in *btd* mutants compared to sibling controls, as inferred from the greater reduction in their apical area (Figure 2e). Taken together, these analyses suggest the expansion of mitotic domains, and the extension of the germ band are potential sources of mechanical stress to the epithelial monolayer, and that they may be involved in the formation of ectopic folds by tissue buckling.

To determine the relative contribution of mitotic domains and germ band as sources of mechanical

stress on the head–trunk boundary, we created a physical model to simulate these tissue mechanics *in silico* and performed experimental perturbations to test our theoretical predictions *in vivo* (see below).

Our model represents an epithelial monolayer confined inside a rigid shell. It embodies one side of a frontal slice between the midline and the dorsal apex of a *Drosophila* embryo with its typical morphological proportions (Figure 3a, Figure S5). The blastoderm is modeled by an elliptical arc of equidistant particles connected by springs and enclosed on one side by a rigid barrier representing the vitelline envelope (Figure 3b). The total energy per unit length of this tissue (W_T) is a sum of a stretching energy component (W_s) and a bending energy component (W_b) (Figure 3c). Each of these components have a rigidity associated with them. K_s is the stretching rigidity and K_b is the bending rigidity. These two parameters can be combined into a single dimensionless bending rigidity, K_b^* (Figure 3c). To simulate the physical interactions between mitotic domains, germ band, and cephalic furrow, we defined the mitotic domains as compressed regions which tend to expand, and the cephalic furrow as a narrow region having an intrinsic negative curvature predisposing the tissue to invaginate (Figure 3b). The germ band in our model is defined by the position of the posterior end of the tissue which is fixed at different fractions of egg length (g) for each simulation (Figure 3b). The effect of germ band extension appears as a global compression in the blastoderm. Finally, to run the simulations we added a ground level of random noise, and iterated the model towards an equilibrium in the total energy of the system.

We first characterized the general properties of the model. In simulations where folds begin to form, the bending energy increases while releasing a larger amount of stretching energy which in turn decreases the total energy of the system over the iterations (Figure 3d). The increase in bending energy coincides with a rapid deepening of the fold. Once the bending energy reaches a peak, the fold continues to deepen, though more gradually, but the number of folds stabilizes and there are rarely changes in the overall folding patterns (Figure 3d, Figure S6a). Folding events are stochastic and can happen at different iterations across different simulations. Also, we are mainly interested in analyzing the initial position and the number of folding events in each simulation. Hence, we used the state of each simulation at the peak of its bending energy as the reference point to compare with other simulations.

To obtain realistic values of the dimensionless bending rigidity K_b^* where the model matches experimental observations, we performed a sweep across the parameter space in mutant conditions (without the cephalic furrow). As expected, the probability of buckling increases with the amount of germ band extension, mainly in lower bending rigidities (Figure 3e, Figure S6b). At 10% germ band extension, we observe a buckling transition in the phase space of softer conditions ($K_b^* \approx 0.7 \times 10^{-4}$), but in stiffer conditions ($K_b^* \approx 1.2 \times 10^{-4}$) the germ band alone, even at its maximum extension, cannot drive the formation of ectopic folds (Figure 3e, Figure S6b). Adding mitotic domains to the simulations changed the phase diagram and dynamics of ectopic folding. We observe that mitotic domains alone can induce ectopic folds in softer conditions ($K_b^* < 1.1 \times 10^{-4}$) and that the number of folds increased for low values of germ band extension (Figure 3f). In addition, the timing of folding with mitotic domains has decreased across iterations in simulations, specially between 0–20% of germ band extension (Figure S6c). These simulations suggest that, depending on the bending rigidity, the germ band or mitotic domains alone can drive ectopic folding, and that their combined action may increase the mechanical instabilities in the blastoderm epithelium. We thus set to test the individual contribution of mitotic domains and germ band to the epithelial instability by performing perturbation experiments *in vivo*.

We first asked whether the extension of the germ band alone can generate ectopic folds. To that end, we generated double-mutant flies lacking both the cephalic furrow and the mitotic domains by combining *btd* mutants with a loss-of-function allele of *cdc25* or *string* (*stg*), a phosphatase that regulates the cell divisions in cleavage cycle 14 of *Drosophila*[15]. In *stg* mutants, the formation of the cephalic furrow and of other morphogenetic movements during early gastrulation occur normally[15] (Figure S7a,b, Video S4, Video S5). Compared to wildtype, the ectopic folds in *stg* mutants are less frequent and pri-

marily appear near the trunk–germ interface (Table 2), which suggests that mitotic domains affects ectopic folding. Indeed, in *btd–stg* double-mutant embryos, we find no ectopic folds forming at the head–trunk interface (Figure 4a,b,j, Video 10, Video 11). The experiment shows that mitotic domains are required for ectopic folding, and the push from the germ band extension alone is insufficient to induce ectopic buckling in cephalic furrow mutants.

To test whether mitotic domains alone are sufficient to induce ectopic buckling *in vivo*, we mechanically blocked the extension of the germ band in cephalic furrow mutants. For that, we cauterized a patch of dorsal tissue, attaching it to the vitelline envelope at the onset of gastrulation (Figure 4c). When the germ band extension is blocked in *btd* and *eve* mutants, no ectopic folds appear at the head–trunk interface (Figure 4c,d,j, Video 7, Video 8, Video 9). Mitotic expansions compress the neighboring non-dividing cells, but no buckling occurs (Figure 4c). Cauterized mutant embryos also show less epithelial deformations compared to non-cauterized mutant embryos (Figure 4d,g). These experiments reveal that *in vivo*, the local expansions of mitotic domains are insufficient to cause epithelial buckling at the head–trunk interface, and that the germ band extension is required.

These *in vivo* experiments show that neither the mitotic domains nor the germ band can promote ectopic folding by themselves. In our model, these situations occur around a bending rigidity of $K_b^* \approx 1.0 \times 10^{-4}$. At this bending rigidity the number of folds falls below 1 in germ band only and mitotic domains only conditions (Figure S6b,c). This suggests that the bending rigidity regime of the epithelium *in vivo* is around the same order of magnitude.

Overall, our *in silico* modeling and *in vivo* experiments suggest that the epithelial buckling at the head–trunk interface in cephalic furrow mutants only occurs when both the mitotic domain expansion and the germ band extension happen concomitantly. This suggests that the combined activity of mitotic domains and germ band extension increases the compressive stresses at the head–trunk boundary during early gastrulation. In conditions where the cephalic furrow formation is perturbed, this leads to more frequent and larger tissue buckling events. Therefore, we hypothesize that the temporary storage of invaginated cells folded in the cephalic furrow may contribute to absorbing these compressive stresses generated by mitotic domains and germ band extension in wildtype conditions.

To explore the role of the cephalic furrow as a mechanical buffer, we analyzed computationally how it interacts with mitotic domains and with the germ band, and how it influences the formation of ectopic folds. In our model, we programmed the cephalic furrow by establishing an intrinsic negative curvature (κ_o^{CF}) to a narrow region of the particle–spring blastoderm that matches the span of the initiator cells *in vivo* (Figure 3a, Figure S5). Using the bending rigidity fine-tuned with the previous simulations and experiments, we ran a parameter sweep for different values of κ_o^{CF} and established a baseline ($\kappa_o^{CF} > 0.3$) where the invagination forms in a robust manner with minimal variability, phenocopying the cephalic furrow *in vivo* (Figure S8a). Since our experiments indicate that the germ band is compressing the head–trunk tissues, we first asked whether the extension of the germ band can influence the depth of the cephalic furrow. To test *in vivo* whether the presence of the germ band impacts the formation of the cephalic furrow, we blocked the germ band extension by cauterization in wildtype embryos. The cephalic furrow forms normally in cauterized embryos indicating that the germ band extension is not required for its formation (Figure 4e,f). We then measured the maximum depth of the cephalic furrow between cauterized and non-cauterized embryos, and found it is 15% shallower after cauterization (Figure 4h). This result needs to be corroborated with a larger sample size, but it provides initial evidence that the germ band extension has a mild influence on the final depth of the cephalic furrow. In addition, we performed a complementary experiment to determine the size of the region under the influence of the cephalic furrow. By laser ablating cell membranes at different distances from initiator cells in early wildtype embryos, we find that the recoil velocity increases with time and decreases with distance, with an approximate range of at least 40µm anterior and posterior to the initiator cells (Figure 4i). This suggests that the cell shortening of initiator cells, which is actively driven by lateral myosin contractility[8], pulls on the adjacent cells and generates

tension in the surrounding tissues. These experiments corroborate the view that cephalic furrow initiation is autonomous and independent of other morphogenetic movements of gastrulation, such as the germ band extension.

Next, we tested the conditions that impact the effectiveness of the cephalic furrow in preventing the formation of ectopic folds. We ran simulations changing the strength of the cephalic furrow, the timing of mitotic domain formation, and the percentage of germ band extension, and quantified the frequency, the position, and the depth of ectopic folds. Without the germ band, the presence of an active invagination at the head–trunk region reduced the variability of ectopic folding in the neighborhood of the cephalic furrow (Figure 3g). This influence of the cephalic furrow on ectopic folds correlates with the strength of the pull, with higher values preventing ectopic folds more effectively (Figure 3g,h, Figure S8b). Curiously, this buffering effect diminished with the extension of the germ band for intermediate values of κ_o^{CF} (Figure S8b). The cephalic furrow becomes shallower and there is an increase in ectopic folds at the posterior region. Only larger κ_o^{CF} values remained effective in preventing ectopic folds at high percentages of germ band extension (Figure S8b). This suggests that in these conditions, the forces generated by the mitotic expansions and by the germ band extension dominate over the infolding pull of the cephalic furrow.

Finally, given that in wildtype embryos the cephalic furrow forms around 15 min before mitotic domains, we asked whether their relative timing of formation may influence the effectiveness of the cephalic furrow. Indeed, when we added a delay to the formation of mitotic domains, the cephalic furrow is more effective in preventing ectopic folding even for lower κ_o^{CF} values and for greater percentages of germ band extension (Figure 3g,h, Figure S8b). Ectopic folds only form in the posterior region near the germ band tip, a position notably similar to where the dorsal folds form in the *Drosophila* embryo *in vivo*. Taken together, our physical model provides a theoretical basis that an early pre-patterned invagination can effectively prevent mechanical instabilities by absorbing compressive stresses in the tissue.

Discussion

Our results provide evidence that the cephalic furrow accomplishes a physical role during the early gastrulation of *Drosophila*. We found that without the cephalic furrow, the epithelium becomes unstable and subject to erratic buckling events. These ectopic folds, unlike the cephalic furrow, form due to extrinsic forces. We identified two main sources of mechanical stress acting at the head–trunk boundary during gastrulation, mitotic domains and germ band. Mitotic cells have been shown to induce epithelial folding in the tracheal placode of flies[16] as well as in intestinal villi of mice[17]. There are two putative mechanisms involved. First, dividing cells in epithelial monolayers generate in-plane outward forces during the elongation phase[18]. Second, dividing cells can undergo basal detachment and shorten along the apical–basal axis, altering the thickness of the epithelium and creating a potential imbalance that facilitates tissue buckling[19]. We believe that both processes, the apical expansion and basal detachment prime the formation of ectopic folds in cephalic furrow mutants. However, we found that mitotic domains alone cannot induce buckling, and that a concomitant compression from the germ band extension is required. Compressive forces are a key mechanism forming epithelial folds in development[3,20], generating mechanical instability in particular when epithelial monolayers are under confinement[21]. In fact, an intraepithelial compressive force is required for tissue buckling during mitotic rounding in the tracheal placode and intestinal villi mentioned above[16,17]. Our data suggest a similar situation is occurring at the head–trunk boundary of cephalic furrow mutants. The synchronized apical expansion of dividing cells in mitotic domains pushes the adjacent non-dividing cells outward, and forms potentially unstable regions of different epithelial thickness, while the germ band extension generates a global compression on the head–trunk interface (Figure 5a,b). In a condition where there is an excess of tissue on the embryonic surface (no cephalic furrow), the increased compressive stresses compromise the stability of the epithelium during gastrulation. This suggests the

head–trunk epithelium is under mechanical stress from the morphogenetic movements of gastrulation in normal development.

Our findings give support to the idea that the cephalic furrow is preventing the build up of these compressive stresses at the head–trunk boundary. The presence of the cephalic furrow abolishes the formation of ectopic folds in sibling controls and in our simulations, suggesting that invaginating tissue out-of-plane is an effective way to alleviate compressive stresses. The pre-patterned position of the initiator cells, and the active cellular mechanisms deployed to drive the cephalic furrow invagination at the onset of gastrulation, anticipates the compressive stresses at the head–trunk boundary. When mitotic domains appear, a significant portion of the head epithelium is already invaginated and the mechanical forces in the tissue are directed to a single, predictable fold. The relative timing of invagination in respect to the other morphogenetic movements is a crucial factor for preventing mechanical instabilities in the tissue. We thus propose that the transient storage created by the cephalic furrow has a stress-absorbing role, contributing to safeguard the integrity of the epithelial monolayer at the head–trunk boundary during gastrulation.

What remains unclear, however, is whether the increased tissue strain, or the buckling itself, have any adverse effects to embryogenesis. An ectopic fold can, for instance, disrupt cell-to-cell interactions or short-range signaling, leading to patterning defects—especially if they occur when tissues are being specified as during gastrulation. Physical compression may also impact the differentiation of tissues since cells can sense and respond to mechanical stimuli with changes in patterning[22]. More generally, variable ectopic buckling may slow down morphogenesis. In this sense, a canalized process forming a single predictable invagination may improve developmental robustness and allow for faster development, bringing an evolutionary advantage for embryos with a pre-patterned head invagination. This raises an intriguing evolutionary question—if the cephalic furrow has a mechanical role in development, did it first evolve in response to these mechanical stresses of gastrulation? If this was the case, we expect the sources of stress (mitotic domains and germ band extension) to be present in the fly lineage before the evolution of the cephalic furrow. Strikingly, that appears to be the case. Mapping the cephalic furrow in the dipteran phylogeny suggests that the cephalic furrow is an evolutionary novelty that evolved after the appearance of mitotic domains and long germ (Steffen Lemke personal communication) (Figure 5c). One putative scenario is that selection for shorter developmental times concatenated the formation of mitotic domains and germ band extension, increasing the mechanical instabilities at the head–trunk boundary (Figure 5d). In this case, mechanical stress may have acted as a selective pressure for the evolution of a pre-patterned head invagination, averting the potential detrimental effects of mechanical instabilities. These speculations, however, require further testing with experiments that prevent cephalic furrow formation without other genetic side effects, as well as a systematic comparative analysis of mitotic domains, germ band extension, and tissue mechanics across the fly phylogeny. Overall, our work proposes that the cephalic furrow plays a mechanical role in absorbing compressive stresses in fly gastrulation, and introduces the cephalic furrow formation as powerful context to test the hypothesis that mechanical interactions within embryonic tissues may play an important role for the evolution of morphogenesis in early development.

Methods

Fly stocks and genetic crossings

To generate fluorescent cephalic furrow mutants, we performed genetic crosses using the loss-of-function alleles *btd*^{XA} (FBal0030657), *eve*^{3} (FBal0003885), *prd*^{4} (FBal0013967), and *stg*^{2} (FBal0247234); the membrane fluorescent marker *Gap43-mCherry* (FBal0258719, gift from Kassiani Skouloudaki); and the green fluorescent balancers *FM7c, Kr-GFP* (FBst0005193), *CyO, twi-GFP* (gift from Akanksha Jain), and *TM3, Kr-GFP* (FBst0005195). We established stable lines balancing the loss-of-function alleles with fluorescent balancers, and used the lack of GFP signal to identify homozygous embryos in our live-imaging recordings. For genes on chromosomes 1 and 2 (*btd*, *eve*, and *prd*), we added the mem-

brane marker on chromosome 3 (*btd*^{XA}*/FM7c, Kr-GFP;; Gap43-mCherry/MKRS* and *eve*^{3}*/CyO, twi-GFP; Gap43-mCherry/MKRS*). For *stg*, which is located on chromosome 3, we recombined the allele with Gap (*Gap43-mCherry, stg*^{2}*/TM3, Kr-GFP*). Since the *btd–stg* double mutant stable line is weak, we imaged the progeny of *btd*^{XA}*/FM7c, Kr-GFP;; Gap43-mCherry, stg*^{2}*/Gap43-mCherry* flies, identifying *btd* homozygozity by the GFP, and *stg* homozygozity by the lack of cell divisions after gastrulation. The wildtype stocks contain the Gap marker in the Oregon-R genetic background. We obtained the founder fly stocks from the Bloomington Drosophila Stock Center and the Kyoto Stock Center and deposited the lines in the MPI-CBG stock collection. The complete list of FlyBase[23] accession numbers and genotypes is available in the project's data repository[24].

Animal husbandry and embryo collection

We maintained the stocks in 50mL hard plastic vials containing fly food and enclosed with a foam lid. They were kept in an incubator with a constant 25℃ temperature and 65% humidity and a 12:12h light cycle. For imaging, we first amplified the stocks in larger 200mL tubes for a few weeks. We then narcotized the flies with CO_2, and transferred them to a cage with a plate attached to one end containing a layer of apple juice agar and a slab of yeast paste on top. The flies were left to acclimatize in the cage for two days before the experiments. To guarantee the embryos are at a similar developmental stage, we exchanged the agar plate once per hour at least twice (pre-lays), and let the flies lay the eggs on the agar for one hour before collecting the plate. After filling the plate with water, we used a brush to release the eggs from the agar and transferred them to a cell strainer with 100µm nylon mesh (VWR). To remove the chorion, we immersed the embryos in 20% sodium hypochlorite solution (Merck 1.05614.2500) for 90s, washed abundantly with water, and proceeded to mounting for live imaging.

Sample mounting for live imaging

We performed most of our live imaging in Zeiss Lightsheet Z.1 microscope using a mounting strategy optimized to increase the throughput of samples in one session. First, we cut a 22x22mm glass coverslip (0.17mm thickness) into 6x15mm strips using a diamond knife, and attached a single strip to a custom sample holder using silicon glue, letting it harden for 15min. We then coated the coverslip strip with a thin layer of heptane glue and let it dry while preparing the embryos. Using a fine brush, we transferred the embryos collected in the cell strainer onto an agar pad, and oriented them manually with a blunt cactus spine under a stereomicroscope. We aligned about 20 embryos in a single line (head to tail) along the main axis of the strip with the left or ventral sides up, depending on the experiment. To attach the embryos to the coverslip, we carefully lowered the sample holder over the agar pad until the glass coated with heptane glue touched the embryos. We placed the sample holder into the microscope chamber filled with water, and rotated it so that the samples are facing the detection objective directly, and the coverslip is orthogonal to the detection objective; this is important to prevent the lightsheet from hitting the glass edges. With the embryos oriented vertically along the coverslip, the lightsheet generated from the illumination objectives coming from the sides only needs to pass through the width of the embryo (about 200µm). This approach gives the best optics for recording lateral and dorsal views and is ideal for live imaging homozygote embryos since they are only about one fourth of the total number of imaged embryos.

Microscopy and acquisition parameters

For lateral datasets, we used a Zeiss 20x/1NA Plan-Apochromat water immersion objective to acquire stacks with 0.28µm XY-resolution and 3µm Z-resolution covering half of the embryo's volume in a single view. This Z-resolution was restored to 1µm during image processing (see below). For dorsal datasets, we used a Zeiss 40x/1NA Plan-Apochromat water immersion objective to acquire stacks with 0.14µm XY-resolution and 3µm Z-resolution covering a volume around in the middle section of the

anterior end of the embryo. We adjusted the time resolution between 45–60s per frame to maximize the number of embryos acquired in one session. To visualize both the membrane signal (mCherry) and the green balancer signal (GFP), we acquired two channels simultaneously using the 488 and 561nm lasers at 3% power with an image splitter cube containing a LP560 dichromatic mirror with SP550 and LP585 emission filters. All recordings were performed at 25℃.

Lightsheet image processing

We converted the raw imaging datasets into individual TIFF stacks for downstream processing using a custom ImageJ macro in Fiji[25,26]. To visualize the presence and dynamics of ectopic folds, we generated 3D renderings of the surface of embryos in lateral recordings using the plugin 3Dscript in Fiji[27]. For analyzing the entire epithelial surface, we first improved the signal-to-noise ratio and z-resolution of lateral datasets from 3µm to 1µm by training a deep learning upsampling model using CARE[28]. Then, we created cartographic projections of the lateral recordings using the ImSAnE toolbox[29] by loading the restored data in MATLAB[30], segmenting the epithelial surface using ilastik[31], and generating 3D cartographic projections of lateral views following a workflow established for fly embryos[32].

Ectopic folding timing and dynamics

To characterize the relative timing of ectopic folding, we annotated the germ band position and the number of frames after the onset of gastrulation at the initial buckling, when the first cells disappear from the surface in the lateral 3D renderings. We defined the onset of gastrulation (T=0) as the moment immediately after the end of cellularization, and immediately before the beginning of the ventral furrow invagination. To visualize the variability of ectopic folding, we manually traced the fold outlines in lateral recordings using Fiji. Because embryos have different sizes, we first used the plugin *bUnwarpJ*[33] (imagej.net/plugins/bunwarpj) to register individual frames and then applied the same transformation to the fold traces for a standardized comparison. We analyzed the dynamics of ectopic folds by measuring the relative angle and tortuosity of the segmented line traces over time, and to visualize the kinetics we generated color-coded temporal projections using the script *Temporal Color Code* (imagej.net/plugins/temporal-color-code) with the perceptually uniform *mpl-viridis* color map (bids.github.io/colormap) bundled in Fiji.

Ectopic folding area and depth

To estimate the folded area in the cephalic furrow and ectopic folds, we annotated the region of the blastoderm before gastrulation that infolded in the cartographic projections using Fiji, and calculated the area correcting the pixel dimensions according to the coordinates in the projection. For the fold depth, we measured the distance between the vitelline envelope to the tip of the fold at the moment of maximum depth in the dorsal recordings. For the analysis of the epithelial surface, we used the plugin *MorphoLibJ*[34] (imagej.net/plugins/morpholibj) to segment, measure, and color-code the cell apical areas, and the plugin *Linear Stack Alignment with SIFT* (imagej.net/plugins/linear-stack-alignment-with-sift) to register cells between timepoints.

Laser cauterization experiments

We performed laser cauterization experiments in two microscope setups, a Luxendo MuVi SPIM with a photomanipulation module and a Zeiss LSM 780 NLO with multiphoton excitation. For the MuVi SPIM, we embedded dechorionated embryos in 2% low-melting agarose and mounted the samples in glass capillaries to obtain *in toto* recordings. We used a pulsed infrared laser 1030–1040nm with 200fs pulse duration and 1.5W power to cauterize the posterior region of the dorsal embryonic surface, attaching the blastoderm to the vitelline envelope. Using a Olympus 20x/1.0NA water immersion objective, we acquired stacks with 0.29µm XY-resolution and 1µm Z-resolution of four different angles every one minute. For the Zeiss microscope, we attached the embryos with the dorsal side down onto coverslips

using heptane glue and immersing in halocarbon oil. We cauterized the embryos sequentially using a near infrared 800nm laser (Chameleon Vision II) through a single pixel line (210nm/px and 100µs/px) around the same dorsal region to block the germ band extension. We used a Zeiss 25x/0.8NA LD LCI Plan-Apochromat glycerol immersion objective to acquire every 2:38min two different planes of the blastoderm, (i) the surface to monitor the germ band extension, and (ii) 40µm deep in the equatorial region to monitor the occurrence of ectopic folding. The stacks had 0.21µm XY-resolution and one minute time resolution. To obtain a quantitative measure of ectopic folding, we analyzed the degree by which the tissues deform between non-cauterized and cauterized mutants using as a proxy the tortuosity of the epithelium outline. For that, we took the profile slices from dorsal recordings and transformed the curved vitelline envelope into a straight line using the *Straighten* tool of ImageJ (Figure S9a). We then cropped a 200×25µm region along the head–trunk interface and applied gaussian blur, thresholding, and edge detection to obtain the epithelium outline for individual timepoints covering about 50min after gastrulation (Figure S9a,b). We extracted measurements from the epithelium outlines using the ImageJ plugin *Analyze Skeleton*[35] (imagej.net/plugins/analyze-skeleton), and generated the color-coded temporal projections as described above.

Laser ablation experiments

We performed laser ablations in a Yokogawa CSU-X1 confocal spinning disk, an EMCCD camera (Andor iXon DU-888), and the software AndorIQ for image acquisition. We attached dechorionated embryos laterally to a MatTek glass-bottom petri dish and covered the samples with water, and performed the ablations using a Titanium Sapphire Chameleon Ultra II (Coherent) laser at 800nm tuned down from 80MHz to 20kHz with a pulse-picker. The laser power measured before the microscope port was 6 mW and the pixel dwell time for scanning was 2µs. To ensure the cut, we repeated the scan ten consecutive times along a single cell acquiring a single slice with a 60x/1.2NA water immersion objective with 0.18µm XY-resolution and 200ms time-steps. We ablated each embryo just once. The temperature was maintained at 28℃. To analyse the ablation data, we created a line crossing the edges of the ablated cell perpendicular to the cut and generated a kymograph using the *Multi Kymograph* Fiji plugin (Figure S10). We then binarized the kymographs, measured the distance between cell edges over the first 30s after the cut, and performed a linear fit of the data to obtain the recoil velocity (Figure S10).

Strain rate analysis

To estimate the strain rates, we first performed particle image velocimetry on cartographic projections using the ImageJ plugin *iterativePIV*[36] (sites.google.com/site/qingzongtseng/piv). Then, we used the equation

$$E = \left| \frac{1}{2}\left(\vec{\nabla}.\vec{v}\right) + \frac{1}{2}\left(\partial_x v_y + \partial_y v_x\right) \right|$$

to define and calculate the magnitude of the strain rate, where v is the displacement obtained in the PIV divided by the time in minutes. The measurements combine isotropic and anisotropic strain rate. We used these values to create a color-coded overlay for the strain rate (Figure S4). To generate the line plots, we averaged the strain rate along the dorsoventral axis in two pre-defined regions, the head–trunk (canonical cephalic furrow position) and the trunk–germ (posterior to the Mitotic Domain 6) (Figure S4).

Model and simulations

Our model follows an approach similar to a previously published model of epithelial buckling under confinement[21]. It represents the monolayer epithelium of the early *Drosophila* embryo in a cross section as a single line through the apical–basal midline of the epithelial cells. The tissue is modeled as an elastic rod with a stretching energy per unit length W_s and bending energy per unit length W_b,

so that the total energy per unit length is $W_T = W_s + W_b$. In full,

$$W_T = \int_{L_o} \frac{1}{2} K_s \left(\frac{ds}{ds_o} - 1 \right)^2 ds_o + \int_{L_o} \frac{1}{2} K_b \left(\kappa - \kappa_o \right)^2 ds_o$$

where K_s is the stretching rigidity and K_b is the bending rigidity of the tissue; ds_o and ds are the preferred and current lengths of the curve, respectively; and κ is the curvature of the rod. L_o is the total length of the tissue in a stress-free condition. To perform numerics, we discretize the curve into N particles indexed by i. The total energy per unit length for this discretized model is given by

$$W_T^* = \frac{1}{2} K_s \sum_{i=2}^{N-3} \left(\frac{\Delta r_i}{\Delta r_o} - 1 \right)^2 \Delta r_o + \frac{1}{2} K_b \sum_{i=2}^{N-3} \left(\kappa_i - \kappa_{o,i} \right)^2 \Delta r_o$$

where Δr_o is the preferred length of springs connecting consecutive points (equal for all springs); Δr_i is the current length between i and $i+1$; κ_i is the discretized curvature at point i; $\kappa_{o,i}$ is the preferred curvature at point i (equal to 0, except when specified). The first and last two points of the curve are fixed in space. To obtain a physically meaningful dimensionless bending rigidity, we divide the bending rigidity by the factor $K_s L^2$ as

$$K_b^* = \frac{K_b}{K_s L^2}$$

where L is the semi-major axis of the embryo. To minimize the total energy, we add a ground level of noise to the particles and let the particles move in the direction of the forces. The motion of the particles are governed by

$$\frac{\Delta \underline{r}_i}{\Delta t} = -\frac{L}{K_s \tau} \frac{\partial W^*}{\partial \underline{r}_i} + \underline{\zeta}_i$$

where $\underline{r}_i$ is the current position of the ith particle; τ represents an arbitrary timescale introduced here to balance dimensions (set to 1); Δt are the timesteps (set to $10^{-5} \times \tau K_s / L$); and $\underline{\zeta}_i$ is the noise, chosen from a gaussian distribution with mean 0 and standard distribution $10^{-5} \times L$. In our model the position of the germ band corresponds to the position of the last particle in the curve on the semi-ellipse that represents the embryonic blastoderm. The extent of the germ band is given by g which is the projection of the germ band arclength onto the mid-axis of the embryo normalized by the embryo length ($2L$). When $g = 0$ the tissue is free of stretching stress, but at any other $0 < g < 1$, the blastoderm will be compressed. The preferred lengths of the individual springs is obtained by dividing the elliptical arclength into N equal segments. The length of each segment is given by $\Delta r_\mathrm{o} = \frac{1}{N} \left(L \int_0^\pi \sqrt{1 - e^2 \cos^2(u)} du \right)$. To find the initial lengths of the springs, we use

$$\Delta r(t=0) = \frac{1}{N} \left(L \int_{u'}^{\pi} \sqrt{1 - e^2 \cos^2(u)} du \right)$$

where $e = \sqrt{1 - (0.4)^2}$; and the angle u' corresponds to the position of the blastoderm end. u' is obtained for a given value of g by $u' = \cos^{-1}(1 - 2g)$. Here, we obtained the initial lengths by dividing the compressed blastoderm into N equal segments. For any simulation, the value of g is constant (blastoderm end is static in position). To model mitotic domains, we introduced new particles and springs on the mid-points between two particles in specific regions of length $0.5L$. The new springs are given the same Δr_o as the rest of the springs in the tissue. The blastoderm is confined by a rigid boundary in the shape of a semi-ellipse. Any particle that lands outside this boundary at any timestep is re-positioned onto the rigid boundary. This new position is prescribed by taking the intersection point of the rigid boundary curve and the line segment that connects the position before this iteration (which was inside or on the vitelline envelope) and the position outside the vitelline envelope. Finally, we define and count a *fold* when we find that a particle's distance from the rigid boundary is greater than a threshold value. To calculate this threshold, we measure the maximum distance that particles can achieve when the tissue is in a stress-free state. This threshold was calculated to be $0.035L$. The code for the model and simulations will be available in a Zenodo repository[37].

Data visualization and figure assembly

For microscopy images, we only performed minimal linear intensity adjustments in microscopy images to improve their contrast and brightness[38]. We created illustrations and assembled the final figure plates using Inkscape v1.2.2[39]. For microscopy videos, we exported the original stacks as AVI without compression with 10–15fps using Fiji and post-processed them to MPEG-4 format 1080p resolution using the H.264 encoding at a constant bitrate quality factor of 18 for visualization using HandBrake v1.6.1[40]. The high-resolution figures and videos are available in a Zenodo repository[41]. We performed the data wrangling, statistical analyses, and plotting in R v4.2.1[42] using RStudio v2022.7.2.576[43], and Python 3.10.7 using Jupyter notebooks[44]. All the data and analyses pipelines were deposited in a Zenodo repository[24].

Data availability

- Data, scripts and analyses[24]:
  - github.com/bruvellu/cephalic-furrow (Git repository)
  - zenodo.org/record/7781948 (Zenodo record)
- Model and simulations[37]:
  - github.com/abhijeetkrishna/cephalic-furrow-theory (Git repository)
  - zenodo.org/record/7784907 (Zenodo record)
- Figures and videos[41]:
  - zenodo.org/record/7784907 (Zenodo record)

Acknowledgements

We thank all current and former LoPaTs for the discussions and support during this project. Akanksha Jain and Vladimir Ulman for initial help with cartographic projections, Giulia Serafini for help with fly crosses, Anaïs Bailles for constructive feedback, and Michaela Burkon and Pavel Mejstrik for technical support. Jan Brugués and Keisuke Ishihara for the laser ablation setup, the MPI-CBG Light Microscopy Facility and Computer Services Facility for the generous support, and Sven Ssykor and Cornelia Maas for help with fly stocks. Steffen Lemke and Yu-Chiun Wang for cephalic furrow discussions. Juliana Roscito for text revisions and support. Michael Akam for drawing BCV's attention to the cephalic furrow. Carles Blanch-Mercader for feedback on simulations. This work was supported by the MPI-CBG core funding to CDM and PT. AS was supported by funding from the European Union's Horizon 2020 Research and Innovation Programme under grant agreement no. 829010 (PRIME). BCV was supported by an EMBO Long Term Fellowship (ALTF 74-2018), and by an European Research Council Advanced Grant (ERC-AdG 885504 GHOSTINTHESHELL) awarded to PT.

Author contributions

BCV and PT conceived the study. BCV designed the experiments, generated the fly stocks, performed the live imaging and image processing, and analysed the data. MBC performed the laser ablations and cauterizations and the strain rate analyses. CDM, AK, and AS designed the model. AK and AS created the model and performed the simulations. BCV wrote the manuscript. All authors revised and contributed to the text.

References

1. Wang, Y.-C. The origin and the mechanism of mechanical polarity during epithelial folding. *Semin. Cell Dev. Biol.* **120,** 94–107 (2021).

2. Denk-Lobnig, M. & Martin, A. C. Divergent and combinatorial mechanical strategies that promote epithelial folding during morphogenesis. *Curr. Opin. Genet. Dev.* **63,** 24–29 (2020).

3. Collinet, C. & Lecuit, T. Programmed and self-organized flow of information during morphogenesis. *Nat. Rev. Mol. Cell Biol.* **22,** 245–265 (2021).

4. Hartenstein, V. & Campos-Ortega, J. A. Fate-mapping in wild-type *Drosophila melanogaster*. *Wilhelm Roux Arch. Entwickl. Mech. Org.* **194,** 181–195 (1985).

5. Foe, V. E. Mitotic domains reveal early commitment of cells in *Drosophila* embryos. *Development* **107,** 1–22 (1989).

6. Spencer, A. K., Siddiqui, B. A. & Thomas, J. H. Cell shape change and invagination of the cephalic furrow involves reorganization of F-actin. *Dev. Biol.* **402,** 192–207 (2015).

7. Vincent, A., Blankenship, J. T. & Wieschaus, E. Integration of the head and trunk segmentation systems controls cephalic furrow formation in *Drosophila*. *Development* **124,** 3747–3754 (1997).

8. Eritano, A. S., Bromley, C. L., Bolea Albero, A., Schütz, L., Wen, F.-L., Takeda, M., Fukaya, T., Sami, M. M., Shibata, T., Lemke, S. & Wang, Y.-C. Tissue-Scale mechanical coupling reduces morphogenetic noise to ensure precision during epithelial folding. *Dev. Cell* **53,** 212–228.e12 (2020).

9. Liu, F., Morrison, A. H. & Gregor, T. Dynamic interpretation of maternal inputs by the *Drosophila* segmentation gene network. *Proc. Natl. Acad. Sci. U. S. A.* **110,** 6724–6729 (2013).

10. Turner, F. R. & Mahowald, A. P. Scanning electron microscopy of *Drosophila melanogaster* embryogenesis. II. Gastrulation and segmentation. *Dev. Biol.* **57,** 403–416 (1977).

11. Costa, M., Sweeton, D. & Wieschaus, E. in *The development of* Drosophila melanogaster (eds. Bate, M. & Arias, A. M.) **1,** 425–465 (Cold Spring Harbor Laboratory Press, 1993).

12. Dicko, M., Saramito, P., Blanchard, G. B., Lye, C. M., Sanson, B. & Étienne, J. Geometry can provide long-range mechanical guidance for embryogenesis. *PLoS Comput. Biol.* **13,** e1005443 (2017).

13. Stern, T., Streichan, S. J., Shvartsman, S. Y. & Wieschaus, E. F. Deconstructing gastrulation at the single cell level. *bioRxiv* 2021.09.16.460711 (2021). doi:10.1101/2021.09.16.460711

14. Blankenship, J. T. & Wieschaus, E. Two new roles for the *Drosophila* AP patterning system in early morphogenesis. *Development* **128,** 5129–5138 (2001).

15. Edgar, B. A. & O'Farrell, P. H. Genetic control of cell division patterns in the *Drosophila* embryo. *Cell* **57,** 177–187 (1989).

16. Kondo, T. & Hayashi, S. Mitotic cell rounding accelerates epithelial invagination. *Nature* **494,** 125–129 (2013).

17. Freddo, A. M., Shoffner, S. K., Shao, Y., Taniguchi, K., Grosse, A. S., Guysinger, M. N., Wang, S., Rudraraju, S., Margolis, B., Garikipati, K., Schnell, S. & Gumucio, D. L. Coordination of signaling and tissue mechanics during morphogenesis of murine intestinal villi: A role for mitotic cell rounding. *Integr. Biol.* **8,** 918–928 (2016).

18. Gupta, V. K., Nam, S., Yim, D., Camuglia, J., Martin, J. L., Sanders, E. N., O'Brien, L. E., Martin, A. C., Kim, T. & Chaudhuri, O. The nature of cell division forces in epithelial monolayers. *J. Cell Biol.* **220,** (2021).

19. Ko, C. S., Kalakuntla, P. & Martin, A. C. Apical constriction reversal upon mitotic entry underlies different morphogenetic outcomes of cell division. *Mol. Biol. Cell* **31,** 1663–1674 (2020).

20. Nelson, C. M. On buckling morphogenesis. *J. Biomech. Eng.* **138,** 021005 (2016).

21. Trushko, A., Di Meglio, I., Merzouki, A., Blanch-Mercader, C., Abuhattum, S., Guck, J., Alessandri, K., Nassoy, P., Kruse, K., Chopard, B. & Roux, A. Buckling of an epithelium growing under spherical confinement. *Dev. Cell* **54,** 655–668.e6 (2020).

22. Heisenberg, C.-P. & Bellaïche, Y. Forces in tissue morphogenesis and patterning. *Cell* **153,** 948–962 (2013).

23. Gramates, L. S., Agapite, J., Attrill, H., Calvi, B. R., Crosby, M. A., Dos Santos, G., Goodman, J. L., Goutte-Gattat, D., Jenkins, V. K., Kaufman, T., Larkin, A., Matthews, B. B., Millburn, G., Strelets, V. B. & the FlyBase Consortium. FlyBase: A guided tour of highlighted features. *Genetics* **220,** iyac035 (2022).

24. Vellutini, B. C., Cuenca, M. B., Krishna, A., Szałapak, A., Modes, C. D. & Tomančák, P. Repository for: Pre-patterned epithelial invagination prevents mechanical instability during fly gastrulation. (2023). doi:10.5281/zenodo.7781948

25. Schindelin, J., Arganda-Carreras, I., Frise, E., Kaynig, V., Longair, M., Pietzsch, T., Preibisch, S., Rueden, C., Saalfeld, S., Schmid, B., Tinevez, J.-Y., White, D. J., Hartenstein, V., Eliceiri, K., Tomancak, P. & Cardona, A. Fiji: An open-source platform for biological-image analysis. *Nat. Methods* **9,** 676–682 (2012).

26. Rueden, C. T., Schindelin, J., Hiner, M. C., DeZonia, B. E., Walter, A. E., Arena, E. T. & Eliceiri, K. W. ImageJ2: ImageJ for the next generation of scientific image data. *BMC Bioinformatics* **18,** 529 (2017).

27. Schmid, B., Tripal, P., Fraaß, T., Kersten, C., Ruder, B., Grüneboom, A., Huisken, J. & Palmisano, R. 3Dscript: Animating 3D/4D microscopy data using a natural-language-based syntax. *Nat. Methods* **16,** 278–280 (2019).

28. Weigert, M., Schmidt, U., Boothe, T., Müller, A., Dibrov, A., Jain, A., Wilhelm, B., Schmidt, D., Broaddus, C., Culley, S., Rocha-Martins, M., Segovia-Miranda, F., Norden, C., Henriques, R., Zerial, M., Solimena, M., Rink, J., Tomancak, P., Royer, L., Jug, F. & Myers, E. W. Content-aware image restoration: Pushing the limits of fluorescence microscopy. *Nat. Methods* **15,** 1090–1097 (2018).

29. Heemskerk, I. & Streichan, S. J. Tissue cartography: Compressing bio-image data by dimensional reduction. *Nat. Methods* **12,** 1139–1142 (2015).

30. Matlab. MATLAB. (2015). at <https://www.mathworks.com/products/matlab.html>

31. Berg, S., Kutra, D., Kroeger, T., Straehle, C. N., Kausler, B. X., Haubold, C., Schiegg, M., Ales, J., Beier, T., Rudy, M., Eren, K., Cervantes, J. I., Xu, B., Beuttenmueller, F., Wolny, A., Zhang, C., Koethe, U., Hamprecht, F. A. & Kreshuk, A. ilastik: Interactive machine learning for (bio)image analysis. *Nat. Methods* (2019). doi:10.1038/s41592-019-0582-9

32. Vellutini, B. C. How to make cartographic projections using ImSAnE. (2022). doi:10.5281/zenodo.7628300

33. Arganda-Carreras, I., Sorzano, C. O. S., Marabini, R., Carazo, J. M., Ortiz-de-Solorzano, C. & Kybic, J. in *Computer vision approaches to medical image analysis* 85–95 (Springer Berlin Heidelberg, 2006). doi:10.1007/11889762_8

34. Legland, D., Arganda-Carreras, I. & Andrey, P. MorphoLibJ: Integrated library and plugins for mathematical morphology with ImageJ. *Bioinformatics* **32,** 3532–3534 (2016).

35. Arganda-Carreras, I., Fernández-González, R., Muñoz-Barrutia, A. & Ortiz-De-Solorzano, C. 3D reconstruction of histological sections: Application to mammary gland tissue. *Microsc. Res. Tech.* **73,** 1019–1029 (2010).

36. Tseng, Q., Duchemin-Pelletier, E., Deshiere, A., Balland, M., Guillou, H., Filhol, O. & Théry, M. Spatial organization of the extracellular matrix regulates cell-cell junction positioning. *Proc. Natl. Acad. Sci. U. S. A.* **109,** 1506–1511 (2012).

37. Krishna, A., Szałapak, A., Vellutini, B. C., Cuenca, M. B., Tomančák, P. & Modes, C. D. Model and simulations for: Pre-patterned epithelial invagination prevents mechanical instability during fly gastrulation. (2023). doi:10.5281/zenodo.7784907

38. Schmied, C. & Jambor, H. K. Effective image visualization for publications - a workflow using open access tools and concepts. *F1000Res.* **9,** 1373 (2020).

39. The Inkscape Project. Inkscape: Open source scalable vector graphics editor. (2003). at <https://inkscape.org>

40. HandBrake Team. HandBrake: HandBrake's main development repository. (2003). at <https://github.com/HandBrake/HandBrake>

41. Vellutini, B. C., Cuenca, M. B., Krishna, A., Szałapak, A., Modes, C. D. & Tomančák, P. Figures and videos for: Pre-patterned epithelial invagination prevents mechanical instability during fly gastrulation. (2023). doi:10.5281/zenodo.7781917

42. R Core Team. R: A language and environment for statistical computing. (1993). at <http://www.r-project.org>

43. RStudio Team. RStudio: Integrated development environment for R. (2011). at <http://www.rstudio.com/>

44. Granger, B. E. & Perez, F. Jupyter: Thinking and storytelling with code and data. *Comput. Sci. Eng.* **23,** 7–14 (2021).

45. Ashburner, M., Golic, K. G. & Hawley, R. S. Drosophila*: A laboratory handbook.* (Cold Spring Harbor Laboratory Press, 2005). at <https://www.worldcat.org/title/drosophila-a-laboratory-handbook/oclc/56324270>

46. Campos-Ortega, J. A. & Hartenstein, V. *The embryonic development of* Drosophila melanogaster. (Springer Berlin Heidelberg, 1985). doi:10.1007/978-3-662-02454-6

47. Jiménez-Guri, E., Wotton, K. R., Gavilán, B. & Jaeger, J. A staging scheme for the development of the moth midge *Clogmia albipunctata*. *PLoS One* **9,** e84422 (2014).

48. Caroti, F., Urbansky, S., Wosch, M. & Lemke, S. Germ line transformation and in vivo labeling of nuclei in Diptera: Report on *Megaselia abdita* (Phoridae) and *Chironomus riparius* (Chironomidae). *Dev. Genes Evol.* **225,** 179–186 (2015).

49. Wotton, K. R., Jiménez-Guri, E., García Matheu, B. & Jaeger, J. A staging scheme for the development of the scuttle fly *Megaselia abdita*. *PLoS One* **9,** e84421 (2014).

Figures

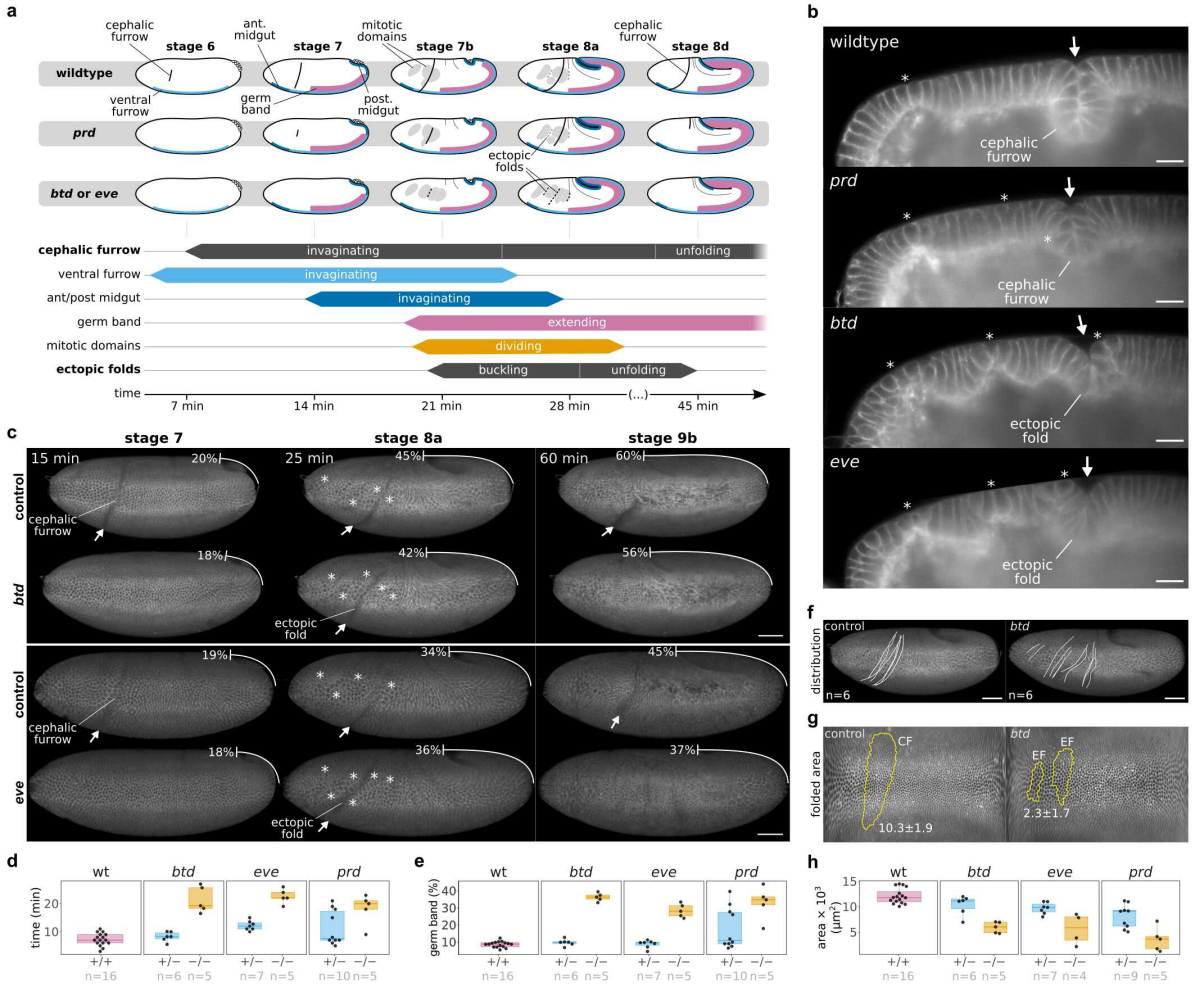

Figure 1: Formation of ectopic folds in cephalic furrow mutants. **a**, Overview of key developmental events using a standard developmental staging[45]. The formation of the cephalic furrow is delayed in *prd* mutants and absent in *btd* and *eve* mutants. In the latter, ectopic folds form near the canonical invagination site of the cephalic furrow. Wildtype and *prd* embryos form less frequent and smaller ectopic folds more anterior or posterior to the cephalic furrow. Ectopic folds appear later and unfold quicker than the cephalic furrow, and their formation coincides with the appearance of mitotic domains and with the rapid phase of the germ band extension[46]. **b**, Profile view of wildtype and *prd* embryos (early stage 8), and *btd* and *eve* embryos (late stage 8) showing the divergent morphology of the cephalic furrow and ectopic folds, respectively. Membrane marker = Gap43-mCherry. Scale bars = 20µm. **c**, Lateral view of sibling controls (heterozygotes) and mutant embryos (*btd* or *eve* homozygotes). The arrows indicate epithelial folds, the asterisks indicate the position of mitotic domains, and the percentages indicate the extent of germ band extension relative to the egg length. Membrane marker = Gap43-mCherry. Scale bars = 50µm. **d**, Timing of formation of cephalic furrow and ectopic folds in different genetic backgrounds. The cephalic furrow forms about 7 minutes after gastrulation in wildtype (+/+, n=16) and *btd* heterozygotes (+/−, n=6), and is delayed in *eve* and *prd* heterozygotes (+/−, n=7 and n=10, respectively) and in *prd* homozygotes (−/−, n=5). Ectopic folds form about 20min after gastrulation in *btd* and *eve* homozygotes (−/−, n=5 and n=5, respectively). One dot represents one embryo. **e**, Percentage of germ band extension at the time of formation of the cephalic furrow and ectopic folds in different genetic backgrounds. The cephalic furrow appears at 10% germ band extension, except in *prd* heterozygotes where it varies up to 40%. Ectopic folds form at 30–35% germ band extension. The n values are the same as in **d**. **f**, Variability in the distribution of the cephalic furrow in sibling controls (*btd* heterozygotes) and of the ectopic folds in *btd* mutants (n=6). Scale bars = 50µm. **g**, Folded area of the cephalic furrow (CF) and ectopic folds (EF) in *btd* embryos. The folded region is outlined in yellow on cartographic projections of a representative sibling control *btd* heterozygote (left) and of a *btd* homozygote (right). The numbers indicate the average folded area for the sample type in $\mu m^2 \times 10^3$. **h**, Quantification of the total folded area of epithelial surface in cephalic furrow mutants.

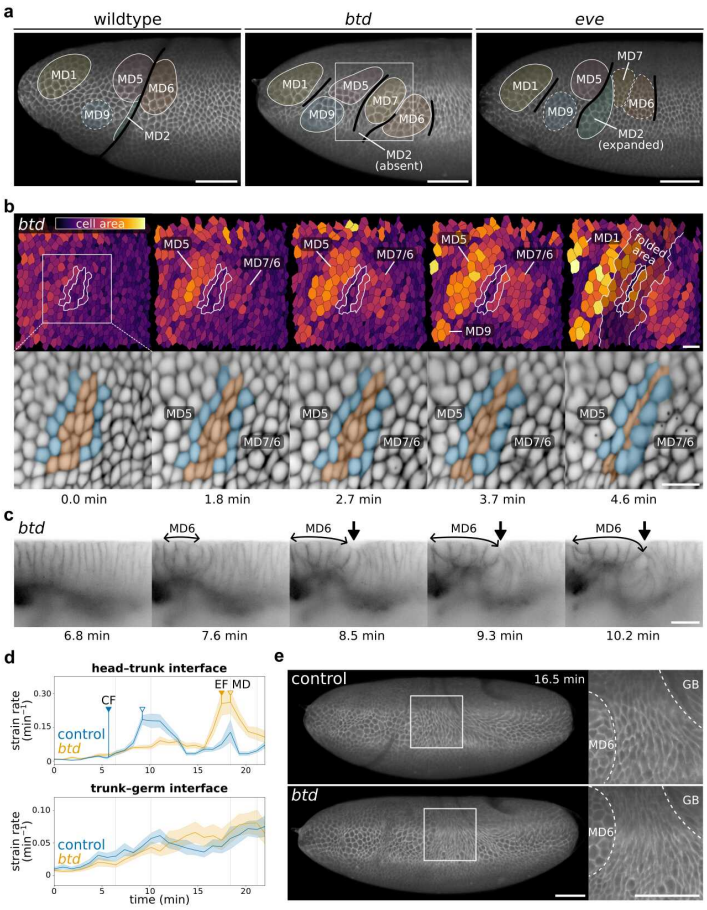

Figure 2: Coincidence of mitotic domains and germ band extension with ectopic folding. **a**, Position of ectopic folds (black lines) in relation to the mitotic domains (colored areas) in *btd* and *eve* mutants. The ectopic folds appear between mitotic domains and between the germ band and the mitotic domain 6 (MD6). Scale bars = 50µm. **b**, Apical cell area between mitotic domains MD5 and MD7/6 (top). The infolded area is highlighted in the last frame (4.6 min). Detail of a cell subset in between mitotic domains (bottom) showing non-dividing cells (orange) and adjacent dividing cells (blue). Scale bars = 20µm (this is an approximate value because the pixel resolutions vary across the projection). **c**, Ectopic folding forming between MD6 and the germ band in a *btd* mutant. Scale bar = 20µm. **d**, Strain rate analysis at the head–trunk (top) and trunk–germ (bottom) regions. The formation of the cephalic furrow (CF), ectopic folds (EF), and mitotic domains (MD) are annotated. The measurements combine isotropic and anisotropic strain rate. **e**, Compressed epithelial cells between MD6 and the tip of the germ band. Scale bars = 50µm.

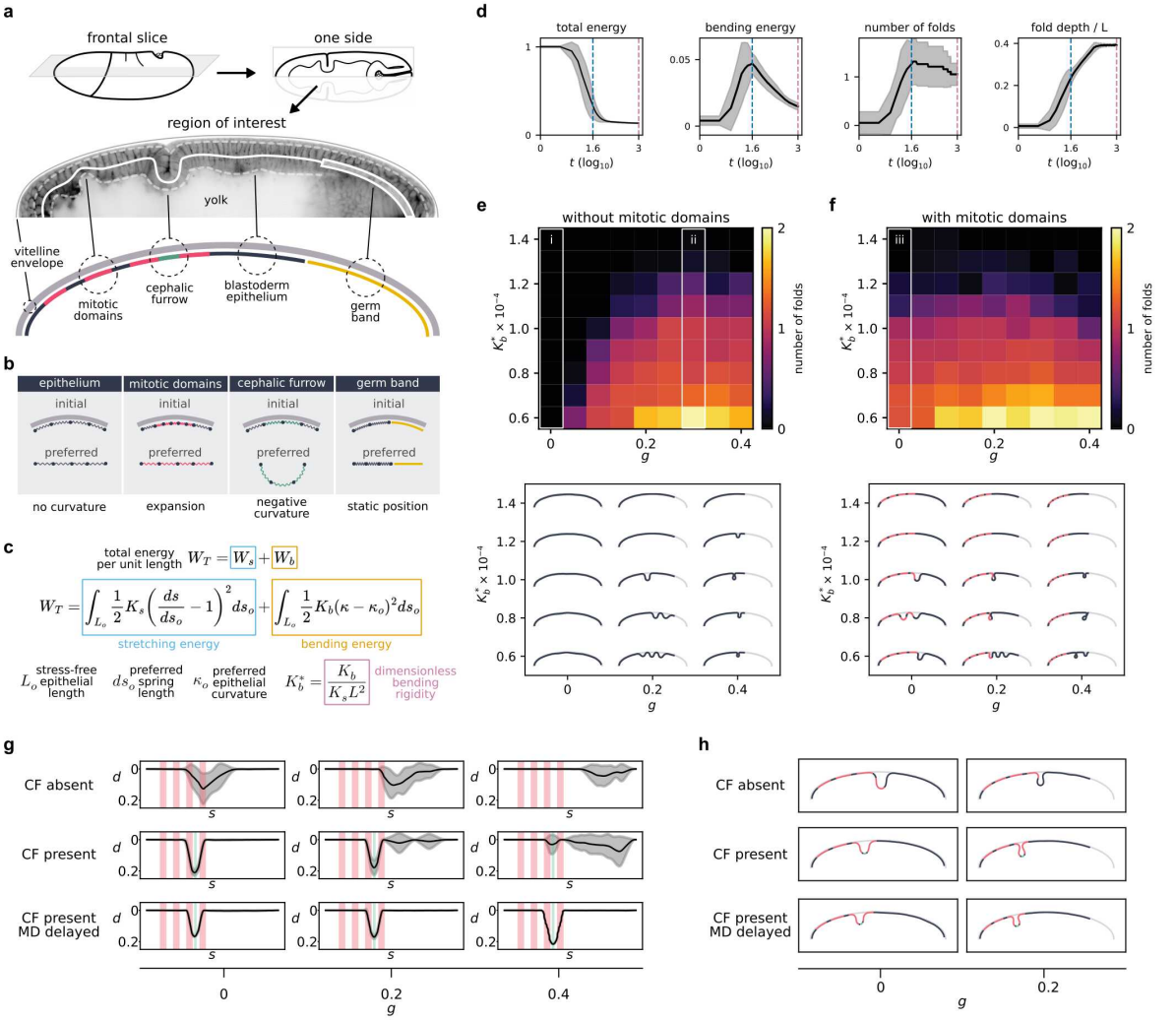

Figure 3: Model and simulations of the tissue mechanics at the head–trunk boundary. **a**, Region of interest of the model. One side of a frontal slice across a slightly dorsal plane of the embryonic blastoderm. It follows the embryo shape, its proportions, and the relative positions of mitotic domains, cephalic furrow, and germ band. **b**, Characteristics of the individual components of the model based on particles connected by springs. The drawings exemplify the initial and final states for each component. **c**, Energy equation with a stretching and a bending component, and the dimensionless bending rigidity. Stress-free rod length (L_o), total energy per unit length (W_T), stretching energy per unit length (W_s), bending energy per unit length (W_b), stretching rigidity (K_s), bending rigidity (K_b), preferred spring length (ds_o), current spring length (ds), preferred curvature (κ_o), current curvature (κ), semi-major embryonic axis (L). **d**, Plots showing the energy dynamics across iterations in a typical simulation run. The total energy goes down to equilibrium. The bending energy increases drastically reaching a peak (blue dashed line) that diminishes gradually with the iterations. Energy values are normalized by the initial total energy. The number of folds stabilizes when the bending energy peaks but the fold depth continues to increase until the last iteration (pink dashed line). **e**, Mutant parameter sweep without mitotic domains (no cephalic furrow). The heatmap shows the average number of ectopic folds for different bending rigidities and percentages of germ band extension. Ectopic folding frequency increases with lower bending rigidities (softer tissue) and with greater values of germ band extension. Outlined in white is the baseline condition with neither mitotic domains nor germ band but only ground level noise (i), and the germ band only condition with higher number of folding events (ii). **f**, Mutant parameter sweep with mitotic domains (no cephalic furrow). The phase diagram shows an increase in number of folds in relation to **e**. The addition of mitotic domains induces the formation of ectopic folds even without germ band extension (iii). **g**, Quantification of ectopic folding to evaluate the effectiveness of the cephalic furrow. The top row shows a control simulating a cephalic furrow mutant condition with mitotic domains and germ band extension. The middle row shows an active cephalic furrow invagination with mitotic domains forming at the same time without delay. The bottom row shows the cephalic furrow with a delay in mitotic domain formation ($t_{MD} = 5$). $t_{MD} = 1$ corresponds to 10^5 computational timesteps. **h**, Representative simulations in **g** at 0 and 20% germ band extension.

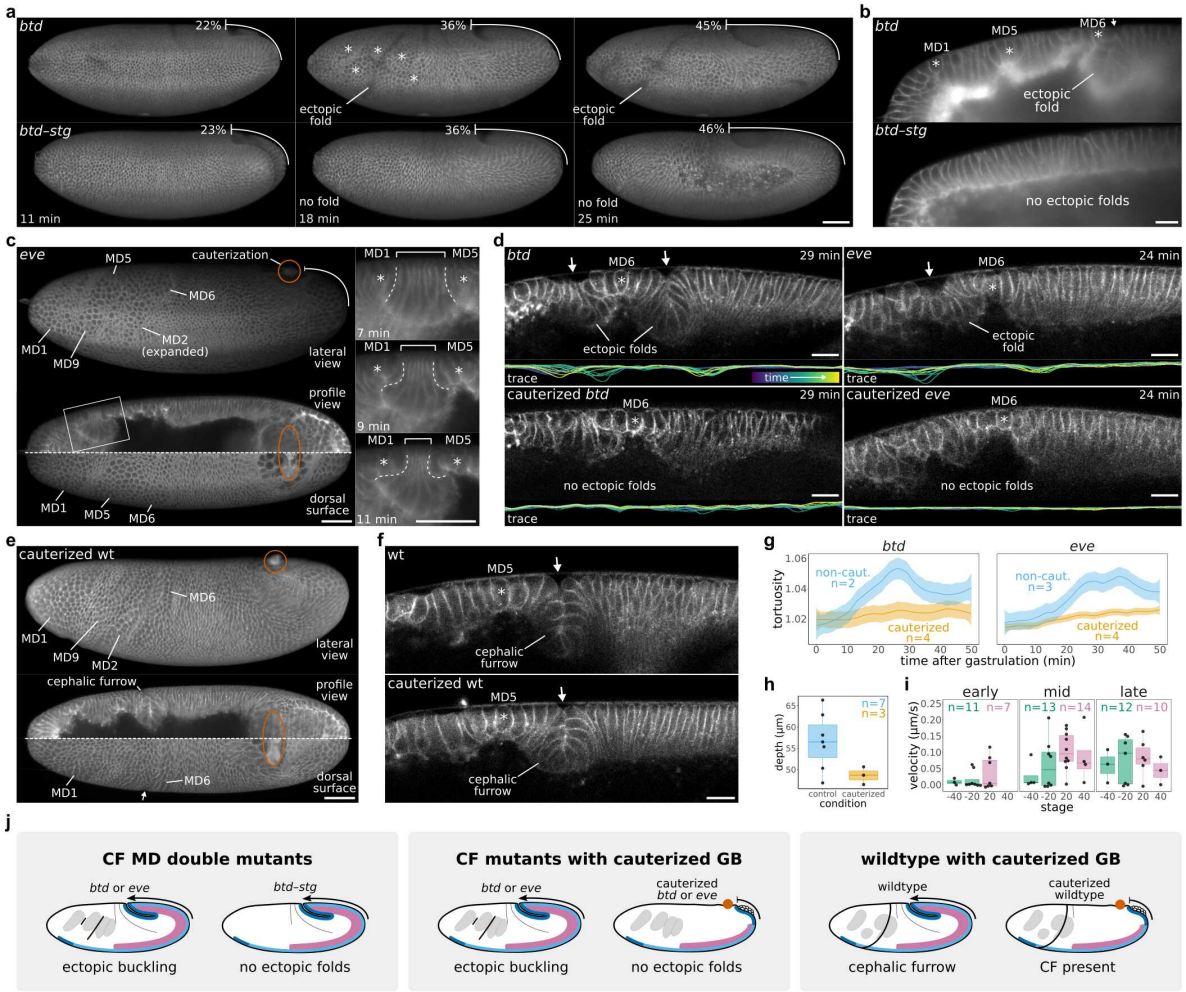

Figure 4: Perturbation experiments *in vivo* using cephalic furrow mutants and wildtype embryos. **a**, Lateral view of *btd–stg* double mutants showing the absence of ectopic folds at the head–trunk boundary compared to a *btd* mutant. Scale bar = 50µm. **b**, Profile view of a *btd–stg* double mutant showing the head–trunk epithelium without mitotic domains or ectopic folds. Scale bar = 20µm. **c**, Cauterized *eve* mutant in lateral (top) and dorsal view (bottom) at the maximum apical expansion of dividing cells in mitotic domains. The cauterization site is marked by a vermilion circle. The boxed outline (right) shows the progressive expansion of mitotic domains compressing the non-dividing cells between MD1 and MD5. Scale bars = 50µm. **d** Profile view and epithelial trace of non-cauterized and cauterized *btd* and *eve* embryos. The trace shows the dynamics of epithelial deformations over time colored from purple to yellow. Cauterized mutants show no ectopic folds and less deformation of the epithelium. Scale bars = 20µm. **e**, Cauterized wildtype embryo in lateral (top) and dorsal view (bottom). The cauterization site is marked by a vermilion circle. The cephalic furrow invaginates normally. Scale bar = 50µm. **f**, Profile view of a non-cauterized and a cauterized wildtype embryo showing a small difference in depth. Scale bar = 20µm. **g**, Tortuosity of the epithelial traces in non-cauterized (*btd* n=2, *eve* n=3) and cauterized (*btd* n=3, *eve* n=4) embryos from **d**. For each embryo, the left and right side were measured. **h**, Maximum depth of the cephalic furrow in cauterized embryos. Control non-cauterized embryos include wildtype (n=2), and *btd* (n=1) and *eve* (n=3) heterozygotes which also form a cephalic furrow. The cauterized group includes wildtype (n=2) and *btd* (n=1). The cephalic furrow in cauterized embryos is 15% shallower (p=0.0221 in Welch Two Sample t-test). **i**, Recoil velocity of laser ablations around the cephalic furrow at stage 6. The average recoil increases with time for anterior cuts (early n=11, mid n=13, late n=12), and reaches a peak at mid stage 6 for posterior cuts (early n=7, mid n=14, late n=10). The average recoil velocity is smaller at greater distances (−40 and 40) than at shorter distances (−20 and 20) from the initiator cells. In late stage 6 the region with recoil reaches at least 40µm anterior and posterior of the invagination. **j**, Schematic drawings showing the summary of the ectopic folding in double mutants and germ band cauterization experiments.

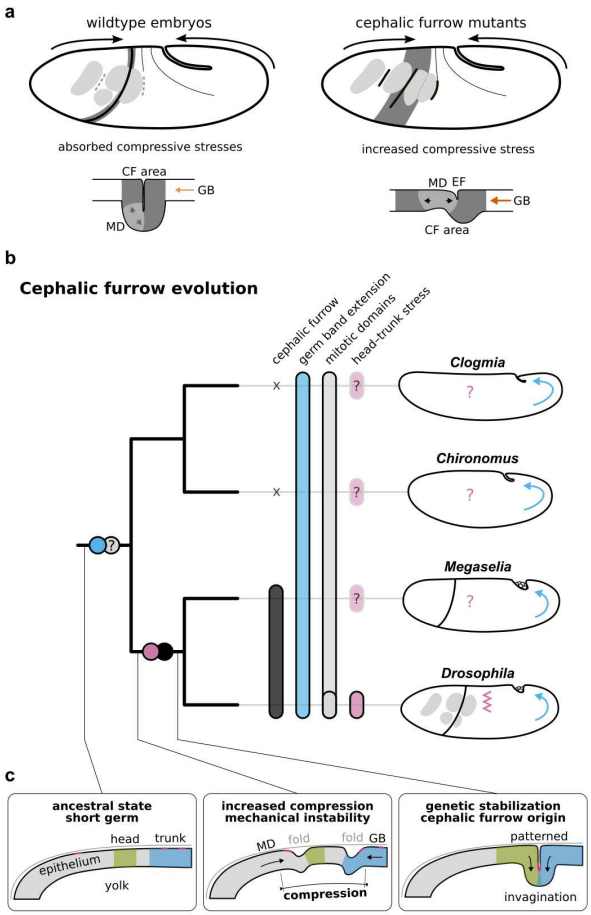

Figure 5: Mechanical role of the cephalic furrow in development and evolution. **a**, Schematic drawings of a lateral view comparing wildtype and cephalic furrow mutants. Tissue flows are represented by black arrows, mitotic domains (MD) by light gray patches, and the cephalic furrow (CF) area by a dark gray band. In cephalic furrow mutants the excess of epithelial tissue on the surface, combined with the formation of mitotic domains and the extension of the germ band (GB), leads to mechanical instabilities and the buckling of ectopic folds (EF) at the head–trunk boundary. **b**, Schematic drawings of a profile view comparing the changes in epithelial thickness in cephalic furrow mutants and the correlation with the position of tissue buckling. **c**, Simplified dipteran phylogenetic tree with mapped traits. The germ band extension and mitotic domains probably evolved at the base of dipteran flies. The cephalic furrow is a late innovation. It is absent in *Clogmia*[47] and *Chironomus*[48], and present in the common ancestor of *Megaselia*[49] and *Drosophila*. It is unclear whether mechanical stresses are present in the head–trunk boundary of flies without cephalic furrow. **d**, Scenario for the evolution of the cephalic furrow. In the ancestral state there was no mechanical instability at the head–trunk boundary. With the evolution of the long germ and mitotic domains there was an increase in the compressive stresses at the head–trunk boundary. Selection for faster developmental times put the region under increased strain leading to the genetic stabilization of a pre-patterned head invagination that buffers these mechanical forces and probably bring a selective advantage to flies with a cephalic furrow.

Videos

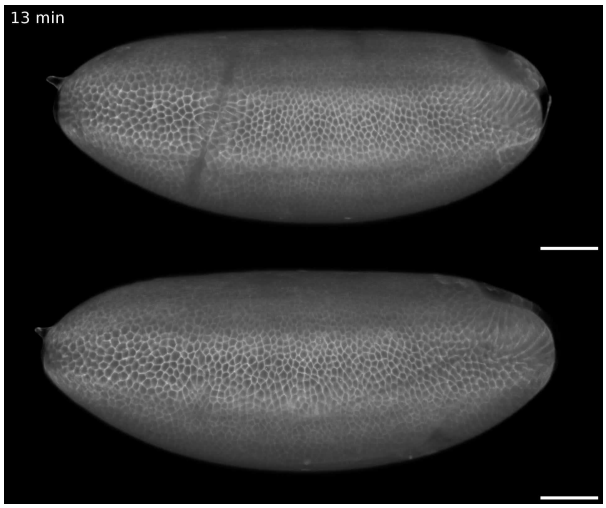

Figure Video 1: Lateral view of ectopic fold formation in *btd* mutant. The cephalic furrow forms normally in sibling controls (top) but it is absent in *btd* mutants (bottom). In the mutant, no fold is present at the head–trunk interface until about 20min, when a large ectopic fold appears and quickly unfolds at about 45min. In the sibling control, the cephalic furrow remains partially invaginated for the period shown in the recording (about 110min). Frame rate = 15fps. Scale bars = 50μm.

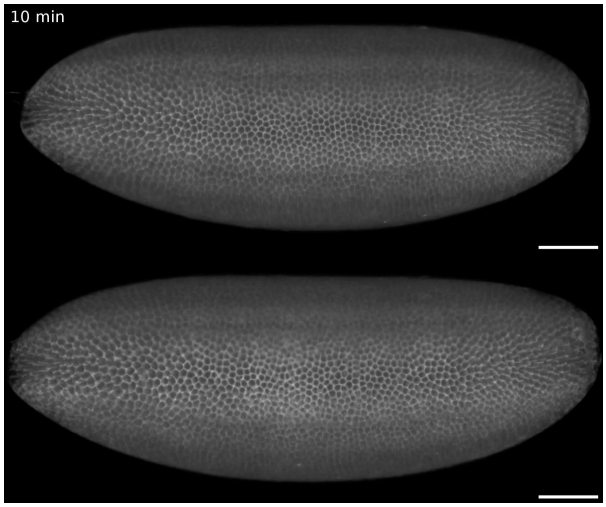

Figure Video 2: Lateral view of ectopic fold formation in *eve* mutant. The cephalic furrow forms normally in sibling controls (top) but it is absent in *eve* mutants (bottom). There is no invagination at the head–trunk boundary at the onset of gastrulation, but an ectopic fold starts forming near the dorsal region as soon as the mitotic domains begin expanding around 24min. The ectopic folds unfolds almost entirely by the end of the recording (about 85min). Additional ectopic folds appear in the trunk region. Frame rate = 10fps. Scale bars = 50µm.

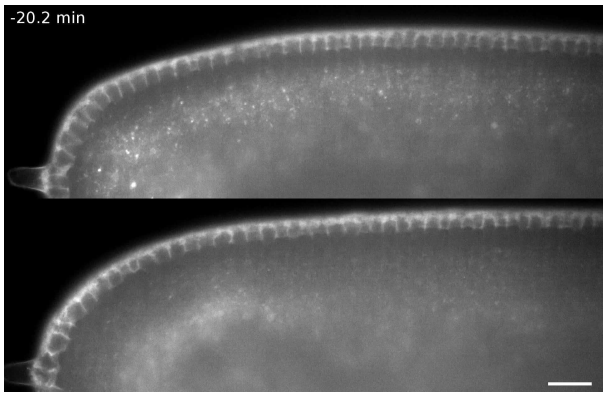

Figure Video 3: Profile view of ectopic fold formation in *btd* mutant. In sibling controls (top), the cephalic furrow initiates at the onset of gastrulation (1.5min) and is fully invaginated when the cell divisions start (about 11min). In *btd* mutants (bottom), no invagination initiates but some embryos exhibit a bulging of the epithelium due to a reminiscent apical constriction behavior (about 7min). An ectopic fold forms at this position. Its morphology differs greatly from the cephalic furrow (see 10min). Both the cephalic furrow and ectopic folds regress with the extension of the germ band. Frame rate = 10fps. Scale bar = 20µm.

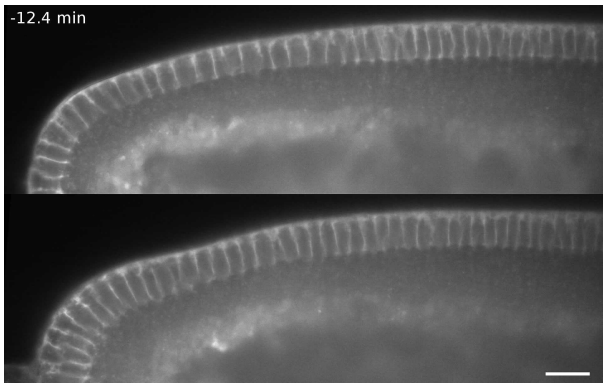

Figure Video 4: Profile view of ectopic fold formation in *eve* mutant. In sibling controls (top), the cephalic furrow intiates at the onset of gastrulation (1.8min). In *eve* mutants, there are no folds appearing in the epithelium until the formation of mitotic domains (about 10min). Then, a large ectopic fold appears posterior to dividing cells (15min). The epithelium of *eve* mutants show additional folding events along the head and trunk regions. Frame rate = 10fps. Scale bar = 20μm.

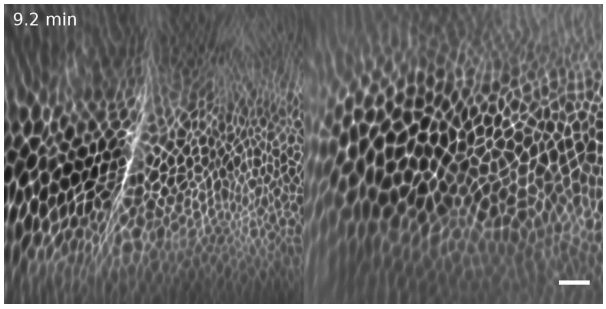

Figure Video 5: Ectopic folding between mitotic domains in *btd* mutant. Detailed view of cartographic projections of *btd* embryos showing the formation of the cephalic furrow (left) and of an ectopic fold (right). In sibling controls, the cephalic furrow initiates in a progressive manner from a narrow row of cells before mitotic domains which only appear at about 20min. In *btd* mutants, the ectopic folds appear in an abrupt manner without any preceding changes in epithelial cells and unfold soon after. Frame rate = 10fps. Scale bar = 20μm (approximate value for cartographic projection).

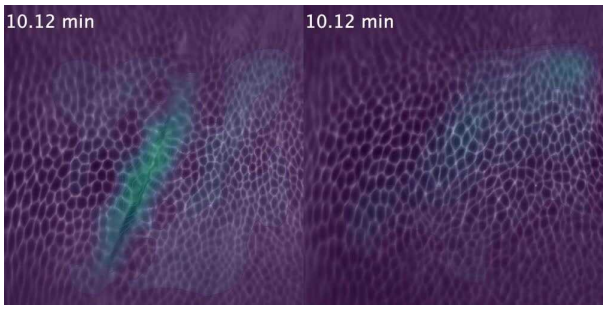

Figure Video 6: Epithelial strain rate during ectopic folding in *btd* mutant. Video from Figure Video 5 overlayed with the estimated strain rate across the tissues (color-coded from purple to yellow). Increase in strain rates are associated with tissue infolding and mitotic expansions. The video is looped. Frame rate = 10fps.

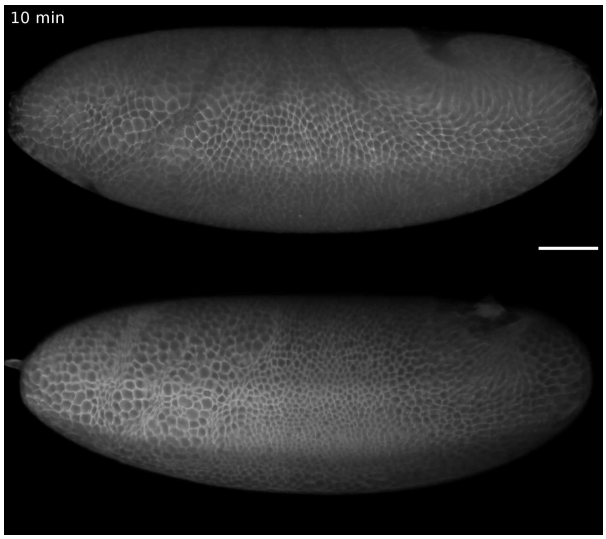

Figure Video 7: Lateral views of germ band cauterization in *eve* embryos. Non-cauterized *eve* embryo showing the formation of ectopic folds (top, same embryo from Figure Video 2) and a cauterized *eve* embryo where no ectopic folds appear at the head–trunk interface (bottom). The germ band extension is mechanically blocked by cauterizing the tissue to the vitelline envelope. Mitotic domains form normally but no folding of the surface occurs. Frame rate = 10fps. Scale bar = 50µm.

Figure Video 8: Profile views of germ band cauterization in *eve* mutant. Same embryo from Figure Video 7, but showing a surface and a profile view. The cauterization prevents the extension of the germ band. The mitotic domains compress non-dividing cells but these do not buckle. Frame rate = 10fps. Scale bar = 50µm.

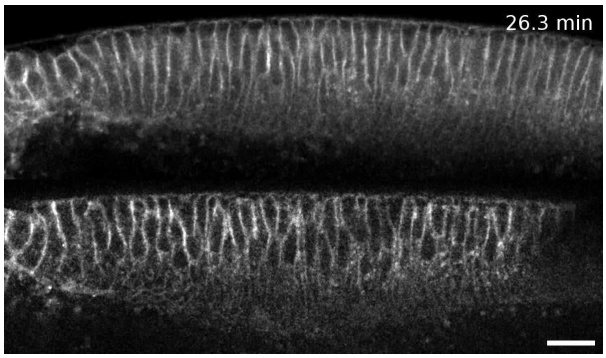

Figure Video 9: Profile views of germ band cauterizations in *btd* embryos. A non-cauterized *btd* embryo (top) showing ectopic folds and a cauterized *btd* embryo showing no ectopic folds (bottom). Frame rate = 10fps. Scale bar = 20µm.

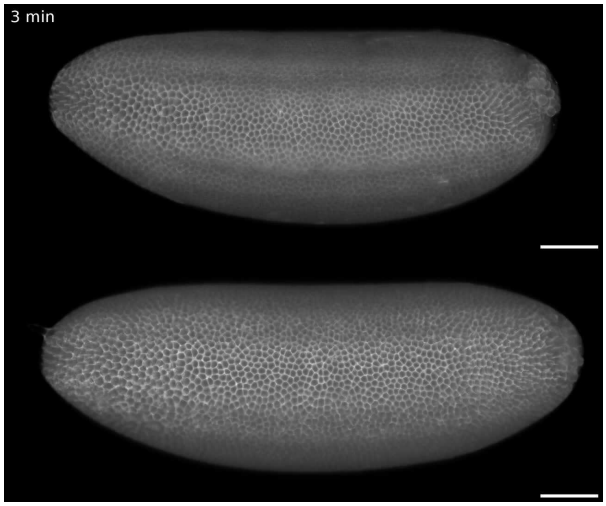

Figure Video 10: Lateral view of *btd–stg* double mutant. A *btd* homozygote (top) shows the formation of ectopic folds while no ectopic folds form in the *btd–stg* double mutant (bottom). Frame rate = 10fps. Scale bars = 50µm.

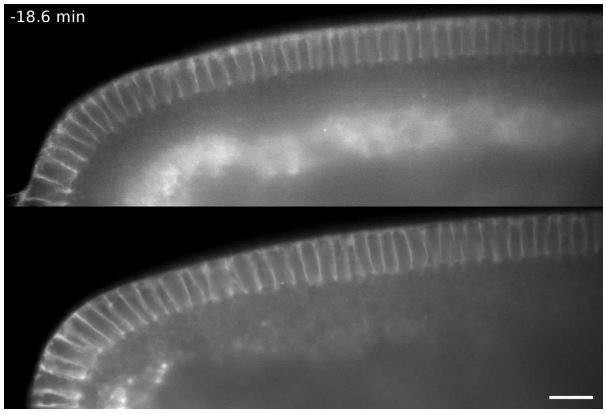

Figure Video 11: Dorsal view of *btd–stg* double mutant. A *btd* homozygote shows the formation of an ectopic fold (top). The *btd–stg* double mutant exhibits no mitotic domains and no ectopic folds (bottom). Frame rate = 10fps. Scale bar = 20µm.

Tables

Table 1: Relative timing differences between the formation of the cephalic furrow (CF) and ectopic folds (EFs) in different mutant backgrounds. We measured the time after gastrulation (TAG) and the percentage of germ band extension (GBE) at the time of infolding/buckling.

	wildtype	*btd*		*eve*		*prd*	
Zygosity	+/+	+/−	−/−	+/−	−/−	+/−	−/−
Fold	CF	CF	EFs	CF	EFs	CF	CF
TAG (min)	7.2±2.2	8.2±1.7	21.3±4.7	12.2±1.7	22.6±2.6	11.3±6.2	18.2±5.4
GBE (%)	8.7±1.7	9.8±1.9	36.3±2.4	8.8±2.3	28.5±3.9	18.0±12.2	33.0±9.5
n	16	6	5	7	5	10	5

Table 2: Number and frequency of ectopic fold formation in cephalic furrow mutants. We calculated the percentage of embryos showing ectopic folds at the head–trunk interface (PEF) and the number of ectopic folds per embryo side (NEF). The *n* includes datasets imaged from the lateral and dorsal sides.

	wildtype	*btd*		*eve*		*prd*		*stg*	
Zygosity	+/+	+/−	−/−	+/−	−/−	+/−	−/−	+/−	−/−
NEF	1.8±0.6	1.1±0.2	2.0±1.0	1.1±0.2	1.8±0.6	1.3±0.5	1.4±0.7	1.2±0.4	1.2±0.4
PEF (%)	80.6	12.9	92.9	12.0	100.0	25.9	42.9	27.3	23.1
n	36	31	14	25	10	27	14	33	13

Table 3: Area of ectopic fold formation in cephalic furrow mutants. We calculated surface area ($\mu m^2 \times 10^3$) of folded cells in the cephalic furrow and ectopic folds of different mutant backgrounds.

	wildtype	*btd*	*eve*	*prd*
CF	11.4±1.2	10.3±1.9	9.7±1.1	6.0±3.4
EF	0.7±0.5	2.3±1.7	3.2±2.1	1.0±0.6
n	CF=16, EF=16	CF=6, EF=13	CF=7, EF=7	CF=14, EF=8

Supplementary information

Figures

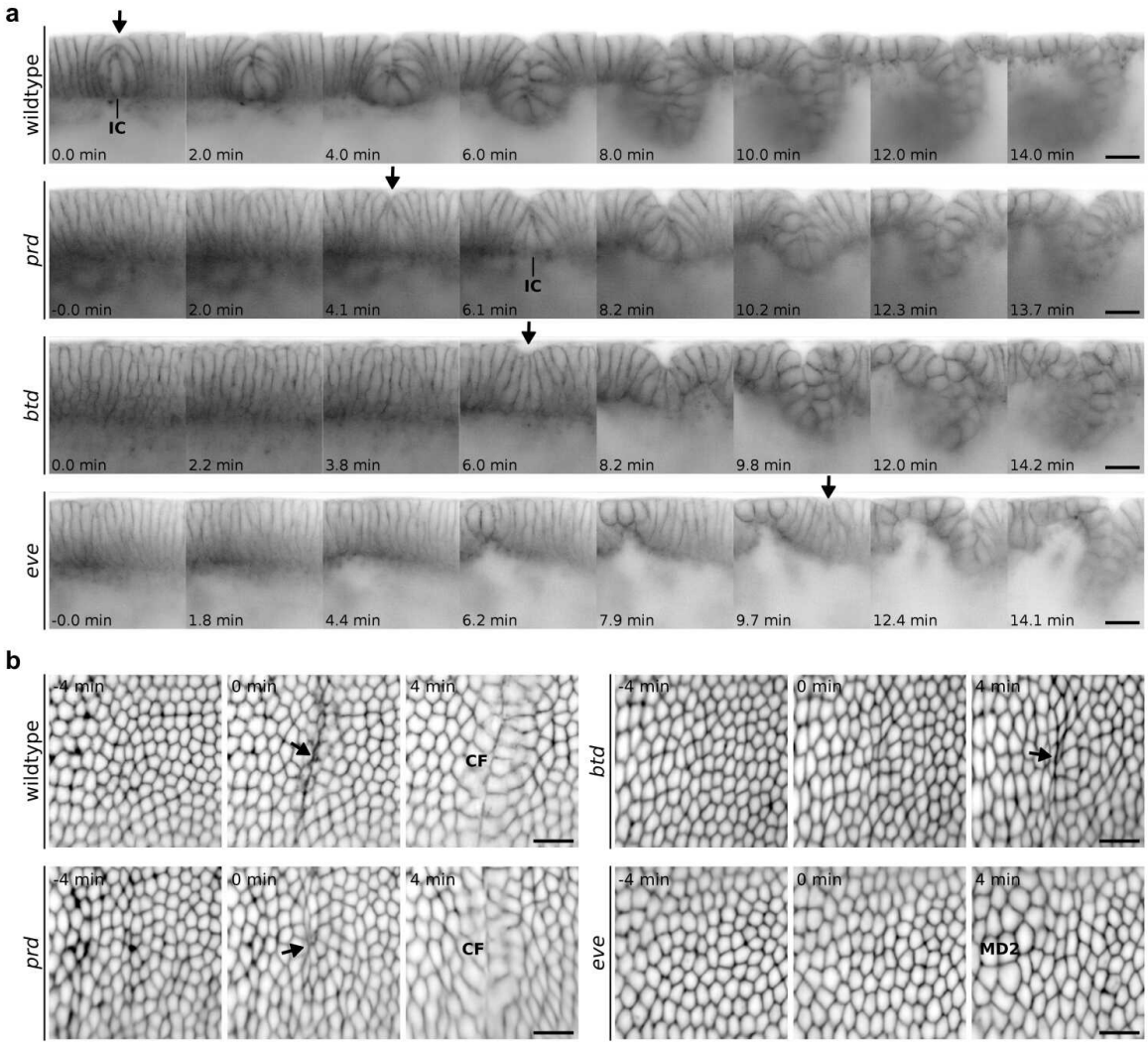

Figure S1: Perturbation of the initiator cell behavior in cephalic furrow mutants. **a**, Profile view showing the cephalic furrow formation in wildtype, *prd*, *btd*, and *eve* embryos. The samples are synchronized by the end of cellularization, when the cleavage furrows reach their basal position (frame 0.0min). The arrow indicates the position and timing of the first infolding of the tissue. In wildtype, the shortening of initiator cells begins before cellularization is complete. The apical side of adjacent cells remain in close contact to the initiator row becoming arched in an arrangement typical for the early phase of cephalic furrow formation (wildtype 0.0min). This arrangement is perturbed in mutant embryos to different degrees. In *prd*, the initiator cells shorten and the tissue invaginates, but the infolding is delayed and the adjacent cells do not arch over the initiator row (*prd* 6.1min). In *btd*, there is no cell shortening but some embryos exhibit a certain degree of anisotropic apical constriction which creates a bulge in the epithelium minutes after the end of cellularization (*btd* 6.0min, see also **b**). This initial bulge often primes the position of ectopic buckling. In *eve*, the cells show neither shortening nor apical constriction and ectopic folds appear about ten minutes after the end of cellularization (*eve* 9.7min). Scale bars = 20µm. **b**, Surface view view of cartographic projections showing the head–trunk interface. In wildtype, the anisotropic apical constriction is localized to a narrow stripe adjacent to the initiator row. In *prd* embryos, the apical constriction occurs but it does not form a clear line of infolding cells preceding the invagination as in wildtype embryos. In *btd* embryos, there is a similar degree of anisotropic apical constriction occurring but not all embryos form ectopic folds at this region. In *eve* embryos, the mitotic domain 2 (MD) begins expanding and there is no apical constriction behavior. Time betwee frames is about 4min. Scale bars = 20µm (approximate value).

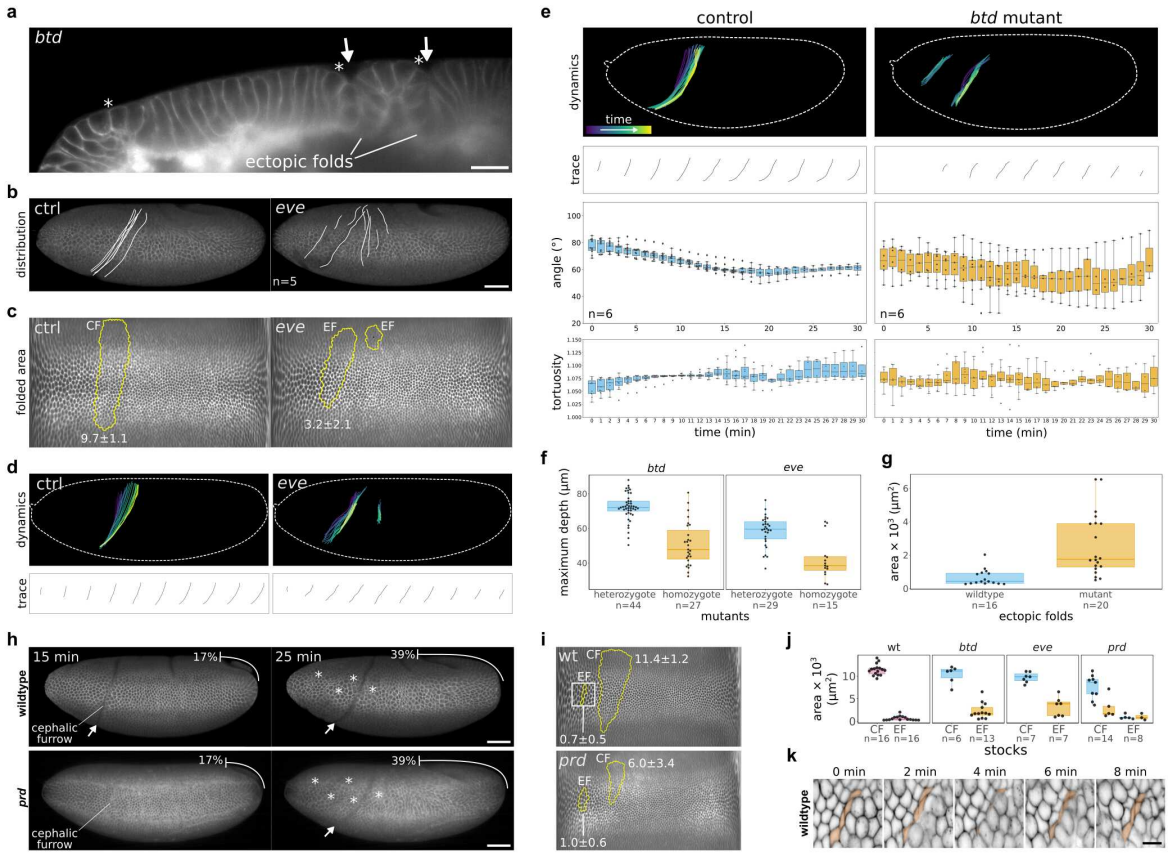

Figure S2: Differences between ectopic folding and cephalic furrow formation. **a**, Profile view of a *btd* mutant embryo showing the presence of two ectopic folds (arrows) forming next to dividing cells (asterisks). Scale bar = 20µm. **b**, Distribution of ectopic folds in *eve* homozygotes (right) and sibling controls (left). Scale bar = 50µm. **c**, Folded area of the cephalic furrow (CF) and ectopic folds (EF) in *eve* embryos. The folded region is outlined in yellow on cartographic projections of a representative sibling control *eve* heterozygote (left) and of a *eve* homozygote (right). The numbers indicate the average folded area for the sample type in $\mu m^2 \times 10^3$. **d**, Dynamics of cephalic furrow and ectopic fold formation in *eve* mutants. **e**, Dynamics, angle directionality, and tortuosity measurements comparing the cephalic furrow and ectopic fold formation. Within the first fifteen minutes after gastrulation, the cephalic furrow exhibits a typical posterior shift on the dorsal side which declines the initial angle of the invagination from 80° to about 60° in relation to the anteroposterior axis. During this period, begins as a straight line and bends showing a correspondent increase in the measured tortuosity values of the furrow outline. In contrast, ectopic folds show no obvious trend in angular direction tortuosity values over time. For both angle and tortuosity analysis, n=6. **f**, Maximum folding depth of the cephalic furrow and ectopic folds in *btd* and *eve* mutants. Ectopic folds are shallower than the cephalic furrow in both genetic backgrounds (*btd* p=1.278e-09 and eve p=9.728e-05 in a Welch Two Sample t-test). Each dot corresponds to a single fold; each embryo can have multiple folds. The number of embryos analyzed for *btd* is 22 heterozygotes and 6 homozygotes, and for *eve* is 14 heterozygotes and 4 homozygotes. **g**, Folded area of ectopic folds in wildtype and mutant embryos (*btd*, *eve*, and *prd*). Ectopic folds in wildtype occupy a smaller area than ectopic folds in cephalic furrow mutants (p=9.107e-06 in a Wilcoxon rank sum exact test). **h**, Lateral views of a wildtype (top) and a *prd* mutant (bottom) exhibiting ectopic folds. Scale bar = 50µm. **i**, Folded area of the cephalic furrow (CF) and ectopic folds (EF) in the wildtype (top) and *prd* mutant (bottom) shown in **h**. The folded region is outlined in yellow on a cartographic projection. The numbers indicate the average folded area in $\mu m^2 \times 10^3$ for the CFs and EFs separately. **j**, Comparison of the folded area between the cephalic furrow and the ectopic folds in different genetic backgrounds. **k**, Developmental sequence of the wildtype embryo ectopic fold annotated in **i**. Four cells are temporarily infolded during the mitotic expansion of adjacent cells. Scale bar = 10µm.

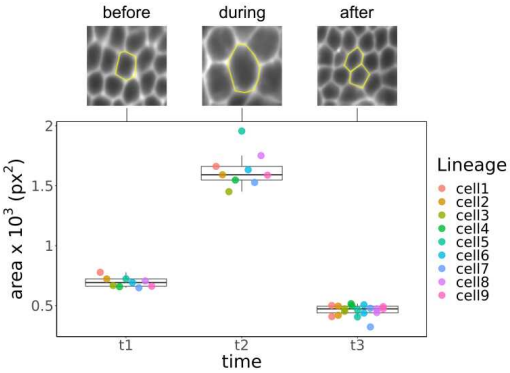

Figure S3: Increase in the apical area of individual cells within mitotic domains. A dividing cell increases its apical area 2.4 times during mitotic rounding. The individual daughter cells retain 66% of the parent apical area. When summed, the apical area of the two daughter cells occupy 1.3 times the original apical area of their parent cell.

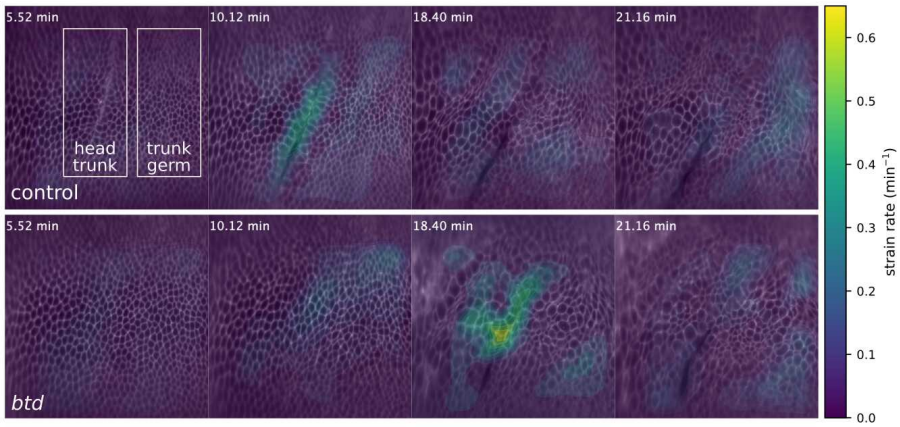

Figure S4: Strain rate analysis in *btd* mutants. Cropped region of cartographic projections of *btd* sibling controls (top, n=3) and homozygote embryos (bottom, n=3). The membrane marker (Gap43-mCherry) is overlayed with a heatmap indicating the regions of increased strain rate in the tissue. The value is the sum of isotropic and anisotropic strain rates obtained through a particle image velocimetry analysis. We used the strain rates in the regions outlined as head–trunk and trunk–germ to generate the plot in Figure 2d.

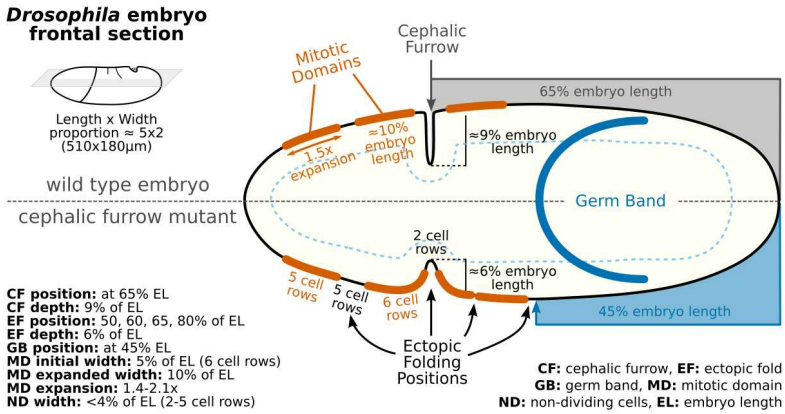

Figure S5: Embryonic proportions in wildtype and cephalic furrow mutants. Approximate relative sizes and positions between embryonic features such as mitotic domains, folds, and the germ band. All values are relative to the embryo length. We used these dimensions as a reference for creating the model.

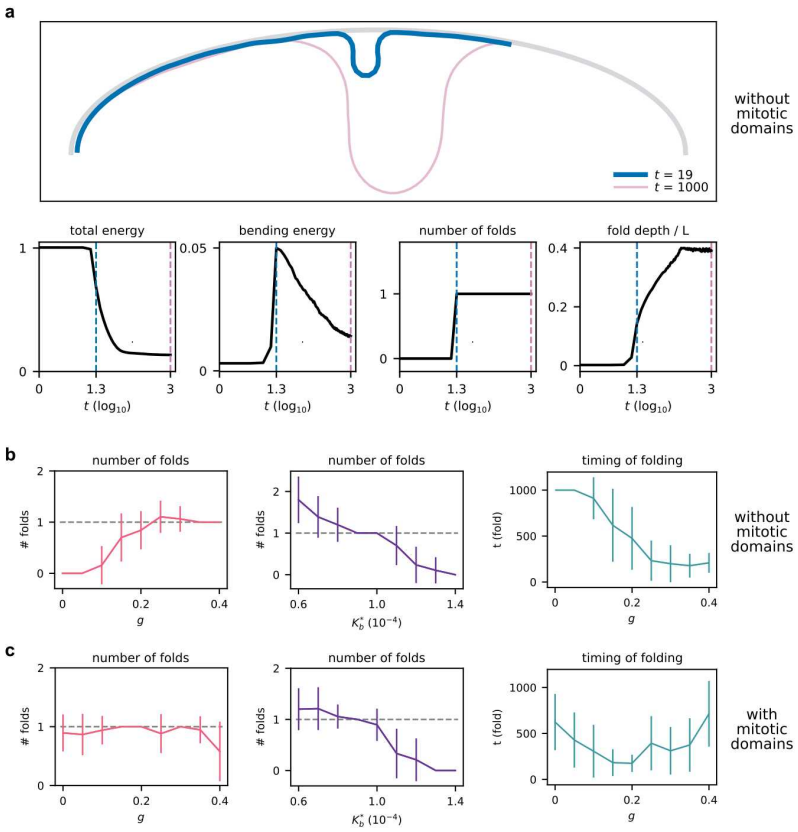

Figure S6: Characterization of the model features. **a**, Representative simulation using $K_b^* = 7 \times 10^{-5}$ and $g = 0.3$ showing the shape of the tissue at $t = 19$ (blue) and $t = 1000$ (pink). The respective timepoints are marked in dashed lines in the descriptive plots below. They show the variation in total energy, bending energy, number of folds, and fold depth over the iterations. $t = 1$ corresponds to 10^5 computational steps and the X axis is in log_{10} scale to improve the visualization. **b**, Parameter sweep without mitotic domains. Plots show the number of folds by germ band extension (g) using $K_b^* = 1.0 \times 10^{-4}$ (left), the number of folds by bending rigidity K_b^* using $g = 0.3$ (center), and the timing of folding by germ band extension (g) using $K_b^* = 1.0 \times 10^{-4}$ (right). **c**, Parameter sweep with mitotic domains. Plots show the same parameters as described in **b** above.

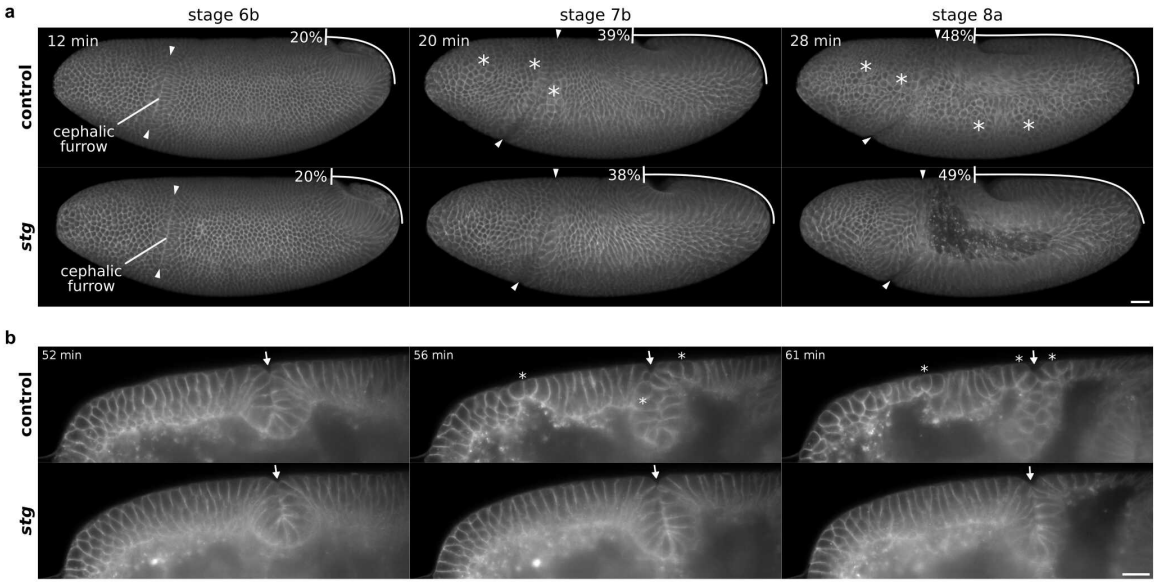

Figure S7: Lateral and dorsal views of *stg* mutant embryos. *stg* homozygotes show no cell divisions after gastrulation but the early morphogenetic movements of gastrulation occur normally. Asterisks indicate mitotic domains. **a**, Lateral 3D renderings. The cephalic furrow forms without delays and exhibits a similar dynamics of invagination compared to wildtype embryos. The only noticeable difference is that the dorsal portion does not shift as posteriorly as in sibling controls, which could be due to the absence of mitotic domains in the head. Scale bar = 50µm. **b**, Profile views. The initiator cell behaviors are not perturbed in *stg* mutants and the morphology of the invagination is intact. In fact, because of the lack of cell divisions, the epithelium remains more uniform during gastrulation when compared to sibling controls or wildtype embryos. Scale bar = 20µm.

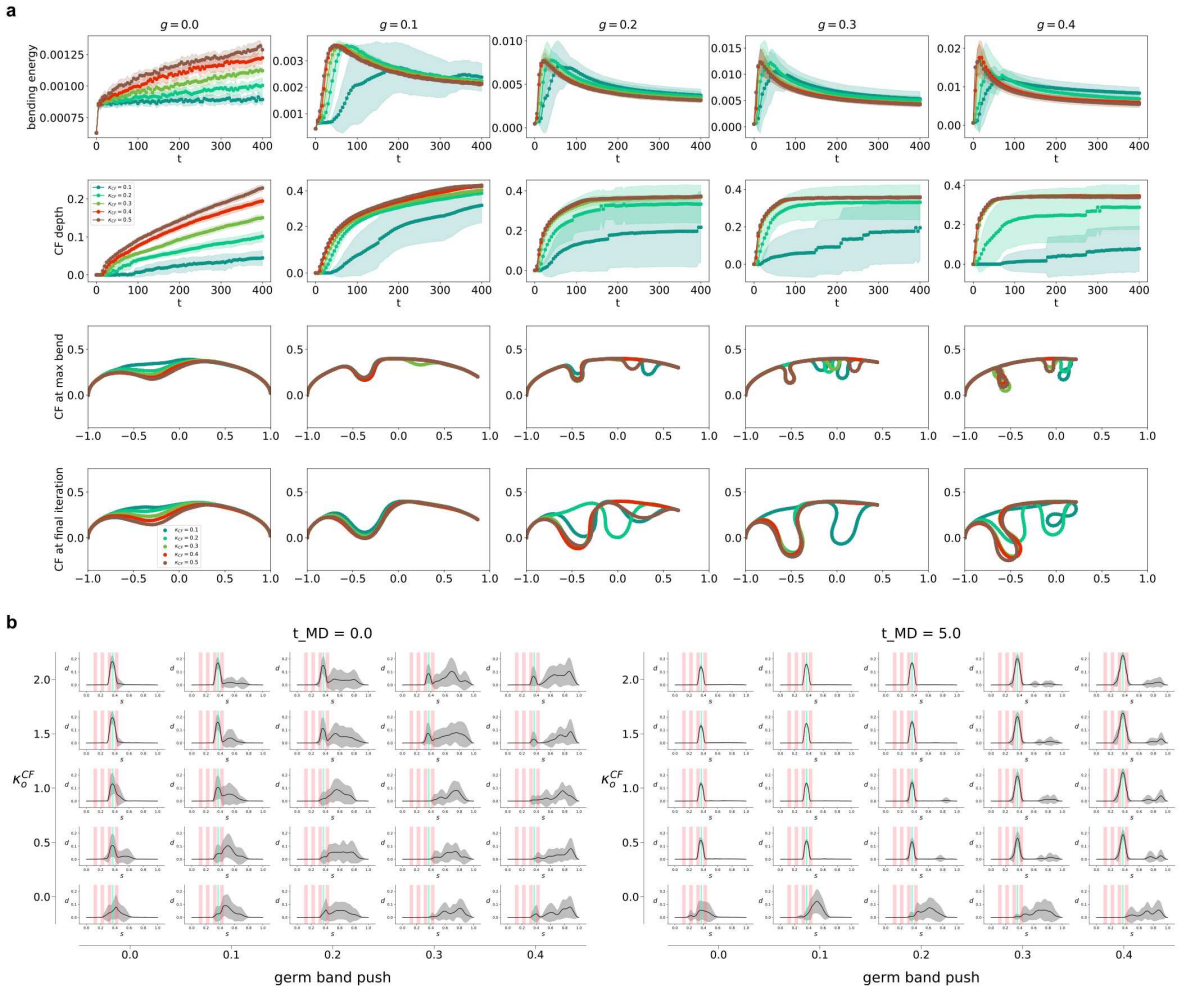

Figure S8: Parameter sweep for cephalic furrow simulations. **a**, Bending rigidity and cephalic furrow depth at different values of κ_o^{CF} and germ band extension. Values above 0.2 exhibit a clear peak in bending energy for most conditions and the depth reaches a plateau across iterations. The cephalic furrow depth at the peak of bending energy (max bend) and at the final iteration is similar for simulations with 0% of germ band extension. At higher percentages of germ band extension the folds (both cephalic furrow and ectopic folds) exhibit a greater depth at the last iteration. **b**, Finer-grained parameter sweep of ectopic folding without ($t_{MD} = 0$) and with ($t_{MD} = 5$) a delay in cephalic furrow formation. With simultaneous formation, only higher values of κ_o^{CF} are effective in buffering the formation of ectopic folds around the cephalic furrow region. This is also limited to low percentages of germ band extension since at higher percentages there is an increase in the frequency of ectopic folding. When a delay in mitotic formation is present, even low values of κ_o^{CF} are effective in preventing the formation of ectopic folds. In this condition, the extension of the germ band increases the formation of ectopic folds, but only at the posterior regions close to the germ band tip. This suggests that the initiation of the cephalic furrow is crucial to its ability to buffer the ectopic folding. Values of κ_o^{CF} are shown in units of $1/L$. $t_{MD} = 1$ corresponds to 10^5 computational timesteps.

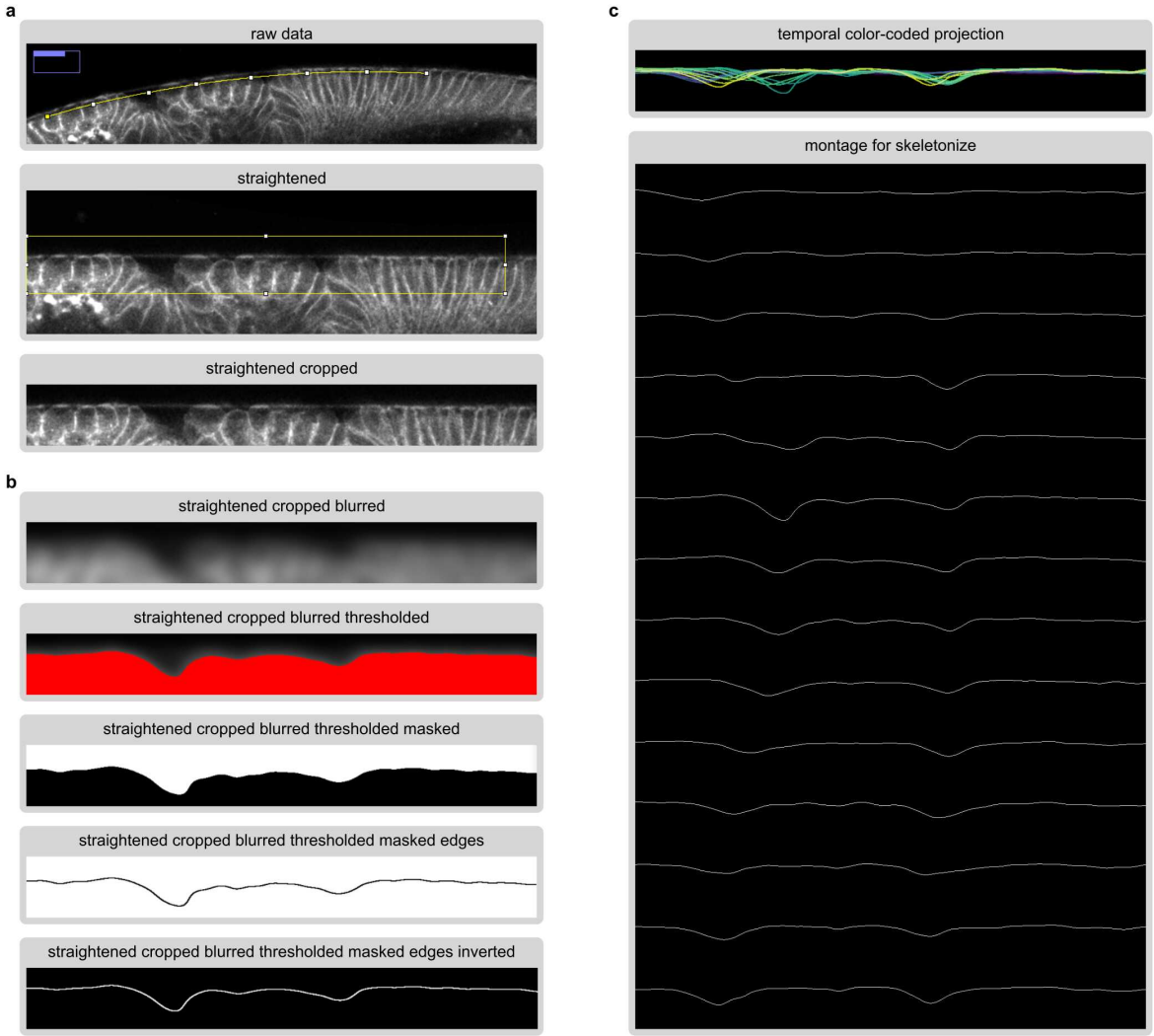

Figure S9: Image processing pipeline for the tortuosity analysis in cauterized mutants. **a**, We acquired a single slice in profile view of the head–trunk epithelium. First, we straightened the epithelial monolayer along the curvature of the vitelline envelope using the Straighten tool in ImageJ. We then cropped a window to standardize the size of the analyzed area for all embryos. **b**, Then, we applied a gaussian blur which allows to capture the deformations in the epithelium caused by the ectopic folds after thresholding. We create a mask and detect edges and invert to retain a single pixel line corresponding to the outline of the epithelium. The image is inverted for downstream processing. **c**, We applied a temporal color-coded projections to visualize the epithelial dynamics over time, and created a montage with all timepoints to extract the length of the outline using the skeletonize plugin in ImageJ.

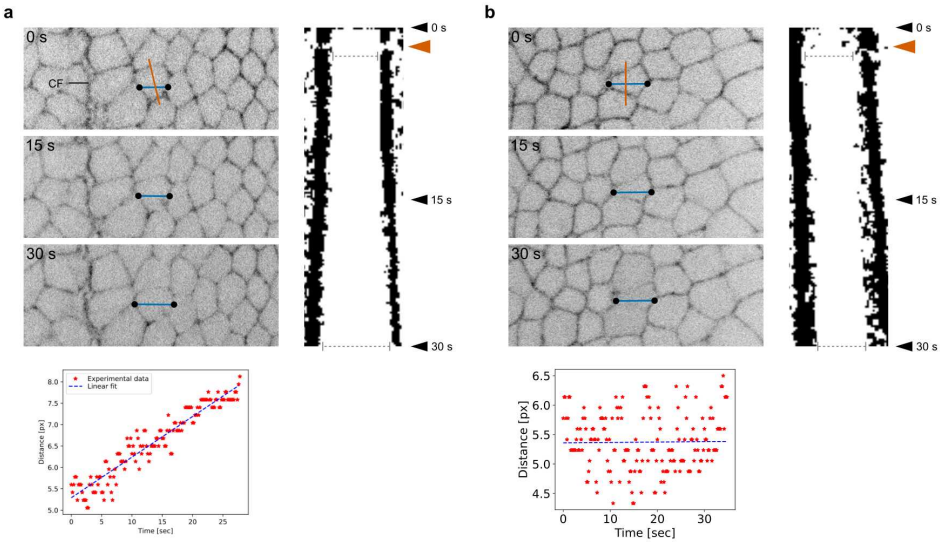

Figure S10: Image processing pipeline for the ablation analysis. **a**, Example of laser ablation near the cephalic furrow with the membrane signal (top left), the generated kymograph (right), and the linear fit over the distance between edges extracted from the kymograph (bottom left). The position of the laser cut is annotated in a vermilion line, the cell edges are marked in black circles, and the edge distances in a blue line. The distance between edges increase over time. **b**, Example of a laser ablation far from the cephalic furrow where the distance between edges does not increase over time.

Videos

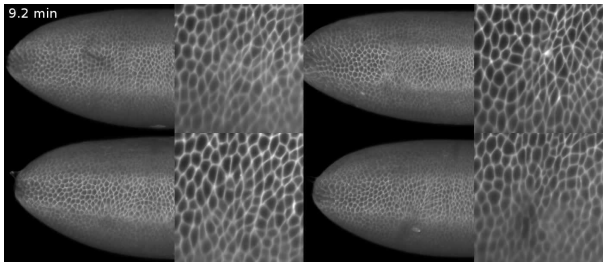

Figure Video S1: Reminiscent apical constriction in *btd* mutants. Lateral view (left) and cartographic projection (right) of the head–trunk interface in four individual *btd* mutants. Cells exhibit different degrees of apical constriction. The video is looped to highlight the changes in apical cell area. Frame rate = 10fps.

Figure Video S2: Dynamics of ectopic folding in *btd* mutant. The cephalic furrow in sibling controls (top) and the ectopic folds in *btd* mutants (bottom) are annotated in white to visualize the dynamics in position, extension, and shape during their formation. Frame rate = 10fps. Scale bars = 50μm.

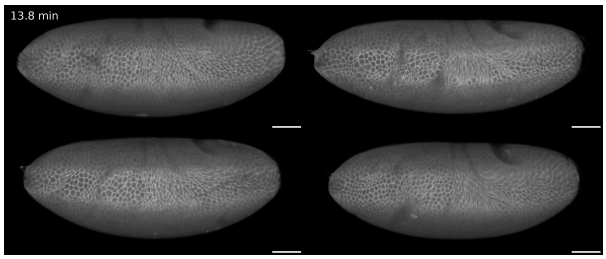

Figure Video S3: Variability of ectopic folding in *btd* mutants. The video shows four individual *btd* mutants where each display a different pattern and number of ectopic folds at the head–trunk interface. The video is looped to highlight the dynamics of ectopic folding. Frame rate = 15fps. Scale bars = 50µm.

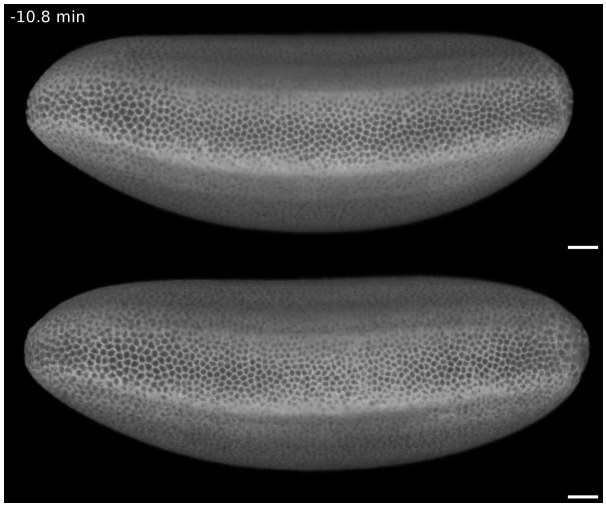

Figure Video S4: Lateral view of cephalic furrow formation in *stg* mutants. Sibling control (top) and *stg* mutant (bottom) during gastrulation. The formation of the cephalic furrow almost identical to the control embryo. The other morphogenetic movements also occur normally until about 35min. At this point the cells in the *stg* mutant are notably larger than the control. Frame rate = 15fps. Scale bars = 50µm.

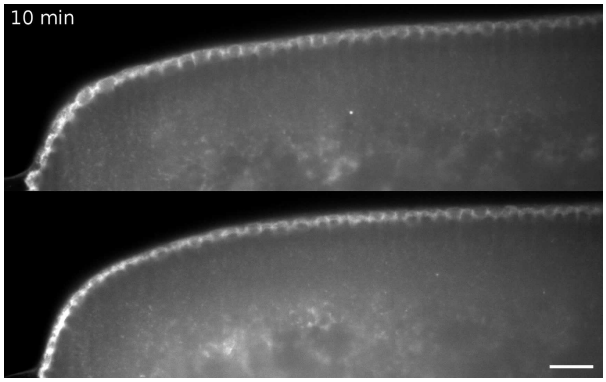

Figure Video S5: Dorsal view of cephalic furrow formation in *stg* mutants. Sibling control (top) and *stg* mutant (bottom) during gastrulation. The cephalic furrow in *stg* mutants initiates without delay and shows identical morphology to the control until cell divisions begin in the latter. The cells dividing within the cephalic furrow of control embryos alter its morphology, it becomes curved and lengthier. In contrast, the cephalic furrow in the *stg* mutant retains its initial morphology until it unfolds. Frame rate = 10fps. Scale bar = 20µm.